

1

<sup>2</sup>A SEARCH FOR LONG-LIVED, CHARGED, SUPERSYMMETRIC PARTICLES  
<sup>3</sup>USING IONIZATION WITH THE ATLAS DETECTOR

4

BRADLEY AXEN

5

September 2016 – Version 0.29

6



<sup>8</sup> Bradley Axen: *A Search for Long-Lived, Charged, Supersymmetric Particles using*  
<sup>9</sup> *Ionization with the ATLAS Detector*, Subtitle, © September 2016

10

Usually a quotation.

11

Dedicated to.



<sub>12</sub> ABSTRACT

---

<sub>13</sub> How to write a good abstract:

<sub>14</sub> <https://plg.uwaterloo.ca/~migod/research/beck00PSLA.html>



<sub>15</sub> PUBLICATIONS

---

<sub>16</sub> Some ideas and figures have appeared previously in the following publications:

<sub>17</sub>

<sub>18</sub> Put your publications from the thesis here. The packages `multibib` or `bibtopic`  
<sub>19</sub> etc. can be used to handle multiple different bibliographies in your document.



---

<sup>21</sup> ACKNOWLEDGEMENTS

<sup>22</sup> Put your acknowledgements here.

<sup>23</sup>

<sup>24</sup> And potentially a second round.

<sup>25</sup>



26 CONTENTS

---

27	I	INTRODUCTION	1
28	1	INTRODUCTION	3
29	II	THEORETICAL CONTEXT	5
30	2	STANDARD MODEL	7
31	2.1	Particles . . . . .	7
32	2.2	Interactions . . . . .	8
33	2.3	Limitations . . . . .	8
34	3	SUPERSYMMETRY	9
35	3.1	Motivation . . . . .	9
36	3.2	Structure . . . . .	9
37	3.3	Phenomenology . . . . .	9
38	4	LONG-LIVED PARTICLES	11
39	4.1	Mechanisms . . . . .	11
40	4.1.1	Examples in Supersymmetry . . . . .	11
41	4.2	Phenomenology . . . . .	11
42	4.2.1	Disimilarities to Prompt Decays . . . . .	11
43	4.2.2	Characteristic Signatures . . . . .	11
44	III	EXPERIMENTAL STRUCTURE AND RECONSTRUCTION	13
45	5	THE LARGE HADRON COLLIDER	15
46	5.1	Injection Chain . . . . .	15
47	5.2	Design and Parameters . . . . .	15
48	5.3	Luminosity . . . . .	15
49	6	THE ATLAS DETECTOR	17
50	6.1	Coordinate System . . . . .	17
51	6.2	Magnetic Field . . . . .	17
52	6.3	Inner Detector . . . . .	17
53	6.3.1	Pixel Detector . . . . .	17
54	6.3.2	Semiconductor Tracker . . . . .	17
55	6.3.3	Transition Radiation Tracker . . . . .	17
56	6.4	Calorimetry . . . . .	17
57	6.4.1	Electromagnetic Calorimeters . . . . .	17
58	6.4.2	Hadronic Calorimeters . . . . .	17
59	6.4.3	Forward Calorimeters . . . . .	17
60	6.5	Muon Spectrometer . . . . .	17
61	6.6	Trigger . . . . .	17
62	6.6.1	Trigger Scheme . . . . .	17
63	6.6.2	Missing Transverse Energy Triggers . . . . .	17
64	7	EVENT RECONSTRUCTION	19
65	7.1	Tracks and Vertices . . . . .	19

66	7.1.1	Track Reconstruction . . . . .	19
67	7.1.2	Vertex Reconstruction . . . . .	19
68	7.2	Jets . . . . .	19
69	7.2.1	Topological Clustering . . . . .	19
70	7.2.2	Jet Energy Scale . . . . .	19
71	7.2.3	Jet Energy Scale Uncertainties . . . . .	19
72	7.2.4	Jet Energy Resolution . . . . .	19
73	7.3	Electrons . . . . .	19
74	7.3.1	Electron Identification . . . . .	19
75	7.4	Muons . . . . .	19
76	7.4.1	Muon Identification . . . . .	19
77	7.5	Missing Transverse Energy . . . . .	19
78	IV	CALORIMETER RESPONSE	21
79	8	RESPONSE MEASUREMENT WITH SINGLE HADRONS	23
80	8.1	Dataset and Simulation . . . . .	24
81	8.1.1	Data Samples . . . . .	24
82	8.1.2	Simulated Samples . . . . .	24
83	8.1.3	Event Selection . . . . .	24
84	8.2	Inclusive Hadron Response . . . . .	25
85	8.2.1	E/p Distribution . . . . .	26
86	8.2.2	Zero Fraction . . . . .	26
87	8.2.3	Neutral Background Subtraction . . . . .	28
88	8.2.4	Corrected Response . . . . .	28
89	8.3	Identified Particle Response . . . . .	34
90	8.3.1	Decay Reconstruction . . . . .	34
91	8.3.2	Identified Response . . . . .	35
92	8.3.3	Additional Species in Simulation . . . . .	37
93	8.4	Summary . . . . .	38
94	9	JET ENERGY RESPONSE AND UNCERTAINTY	41
95	9.1	Motivation . . . . .	41
96	9.2	Uncertainty Estimate . . . . .	41
97	9.3	Summary . . . . .	44
98	V	SEARCH FOR LONG-LIVED PARTICLES	47
99	10	LONG-LIVED PARTICLES IN ATLAS	49
100	10.1	Overview and Characteristics . . . . .	49
101	10.2	Simulation . . . . .	49
102	11	EVENT SELECTION	51
103	11.1	Trigger . . . . .	52
104	11.2	Kinematics and Isolation . . . . .	52
105	11.3	Standard Model Rejection . . . . .	56
106	11.4	Ionization . . . . .	58
107	11.4.1	Mass Estimation . . . . .	59
108	11.5	Efficiency . . . . .	60
109	12	BACKGROUND ESTIMATION	63

110	12.1	Background Sources . . . . .	63
111	12.2	Prediction Method . . . . .	64
112	12.3	Validation . . . . .	65
113	12.3.1	Closure in Simulation . . . . .	65
114	12.3.2	Validation Region in Data . . . . .	65
115	13	SYSTEMATIC UNCERTAINTIES AND RESULTS	67
116	13.1	Systematic Uncertainties . . . . .	67
117	13.2	Final Yields . . . . .	67
118	14	INTERPRETATION	69
119	14.1	Cross Sectional Limits . . . . .	69
120	14.2	Mass Limits . . . . .	69
121	14.3	Context for Long-Lived Searches . . . . .	69
122	<b>VI</b>	<b>CONCLUSIONS</b>	71
123	15	SUMMARY AND OUTLOOK	73
124	15.1	Summary . . . . .	73
125	15.2	Outlook . . . . .	73
126	<b>VII</b>	<b>APPENDIX</b>	75
127	A	INELASTIC CROSS SECTION	77
128	B	APPENDIX TEST	79
129	B.1	Appendix Section Test . . . . .	79
130	B.1.1	Appendix Subection Test . . . . .	79
131	B.2	A Table and Listing . . . . .	79
132	B.3	Some Formulas . . . . .	80
133	BIBLIOGRAPHY		83

134 LIST OF FIGURES

---

135	Figure 1	The particle content of the Standard Model (SM). . . . .	8
136	Figure 2	An illustration (a) of the $E/p$ variable used throughout this paper. The red energy deposits come from the charged particle targeted for measurement, while the blue energy deposits are from nearby neutral particles and must be subtracted. The same diagram (b) for the neutral-background selection, described in Section 8.2.3.	25
137			
138			
139			
140			
141			
142	Figure 3	The $E/p$ distribution and ratio of simulation to data for isolated tracks with (a) $ \eta  < 0.6$ and $1.2 < p/\text{GeV} < 1.8$ and (b) $ \eta  < 0.6$ and $2.2 < p/\text{GeV} < 2.8$ . . . . .	26
143			
144			
145	Figure 4	The fraction of tracks as a function (a, b) of momentum, (c, d) of interaction lengths with $E \leq 0$ for tracks with positive (on the left) and negative (on the right) charge. . . . .	27
146			
147			
148			
149	Figure 5	$\langle E/p \rangle_{\text{BG}}$ as a function of the track momentum for tracks with (a) $ \eta  < 0.6$ , (b) $0.6 <  \eta  < 1.1$ , and as a function of the track pseudorapidity for tracks with (c) $1.2 < p/\text{GeV} < 1.8$ , (d) $1.8 < p/\text{GeV} < 2.2$ . . . . .	29
150			
151			
152			
153	Figure 6	$\langle E/p \rangle_{\text{COR}}$ as a function of track momentum, for tracks with (a) $ \eta  < 0.6$ , (b) $0.6 <  \eta  < 1.1$ , (c) $1.8 <  \eta  < 1.9$ , and (d) $1.9 <  \eta  < 2.3$ . . . . .	30
154			
155			
156	Figure 7	$\langle E/p \rangle_{\text{COR}}$ calculated using LCW-calibrated topological clusters as a function of track momentum for tracks with (a) zero or more associated topological clusters or (b) one or more associated topological clusters. . . . .	31
157			
158			
159			
160	Figure 8	Comparison of the $\langle E/p \rangle_{\text{COR}}$ for tracks with (a) less than and (b) greater than 20 hits in the TRT. . . . .	32
161			
162	Figure 9	Comparison of the $\langle E/p \rangle_{\text{COR}}$ for (a) positive and (b) negative tracks as a function of track momentum for tracks with $ \eta  < 0.6$ . . . . .	32
163			
164			
165	Figure 10	Comparison of the $E/p$ distributions for (a) positive and (b) negative tracks with $0.8 < p/\text{GeV} < 1.2$ and $ \eta  < 0.6$ , in simulation with the FTFP_BERT and QGSP_BERT physics lists. . . . .	33
166			
167			
168			
169	Figure 11	Comparison of the response of the hadronic calorimeter as a function of track momentum (a) at the EM-scale and (b) after the LCW calibration. . . . .	33
170			
171			
172	Figure 12	Comparison of the response of the EM calorimeter as a function of track momentum (a) at the EM-scale and (b) with the LCW calibration. . . . .	34
173			
174			

175	Figure 13	The reconstructed mass peaks of (a) $K_S^0$ , (b) $\Lambda$ , and (c) $\bar{\Lambda}$ candidates. . . . .	35
176			
177	Figure 14	The $E/p$ distribution for isolated (a) $\pi^+$ , (b) $\pi^-$ , (c) proton, and (d) anti-proton tracks. . . . .	36
178			
179	Figure 15	The fraction of tracks with $E \leq 0$ for identified (a) $\pi^+$ and $\pi^-$ , and (b) proton and anti-proton tracks . . . . .	36
180			
181	Figure 16	The difference in $\langle E/p \rangle$ between (a) $\pi^+$ and $\pi^-$ (b) $p$ and $\pi^+$ , and (c) $\bar{p}$ and $\pi^-$ . . . . .	37
182			
183	Figure 17	$\langle E/p \rangle_{\text{COR}}$ as a function of track momentum for (a) $\pi^+$ tracks and (b) $\pi^-$ tracks. . . . .	38
184			
185	Figure 18	The ratio of the calorimeter response to single parti- cles of various species to the calorimeter response to $\pi^+$ with the physics list FTFP_BERT. . . . .	38
186			
187	Figure 19	The spectra of true particles inside anti- $k_t$ , $R = 0.4$ jets with (a) $90 < p_T/\text{GeV} < 100$ , (b) $400 < p_T/\text{GeV} <$ $500$ , and (c) $1800 < p_T/\text{GeV} < 2300$ . . . . .	42
188			
189	Figure 20	The jet energy scale ( $\text{JES}$ ) uncertainty contributions, as well as the total $\text{JES}$ uncertainty, as a function of jet $p_T$ for (a) $ \eta  < 0.6$ and (b) $0.6 <  \eta  < 1.1$ . . . . .	44
190			
191	Figure 21	The $\text{JES}$ correlations as a function of jet $p_T$ and $ \eta $ for jets in the central region of the detector. . . . .	45
192			
193	Figure 22	The distribution of $E_T^{\text{miss}}$ for data and simulated signal events, after the trigger requirement. . . . .	53
194			
195	Figure 23	The dependence of $dE/dx$ on $N_{\text{split}}$ in data after basic track hit requirements have been applied. . . . .	54
196			
197	Figure 24	The distribution of $dE/dx$ with various selections ap- plied in data and simulated signal events. . . . .	55
198			
199	Figure 25	The distribution of track momentum for data and sim- ulated signal events, after previous selection require- ments have been applied. . . . .	55
200			
201	Figure 26	The distribution of $M_T$ for data and simulated sig- nal events, after previous selection requirements have been applied. . . . .	56
202			
203	Figure 27	The distribution of summed tracked momentum within a cone of $\Delta R < 0.25$ around the candidate track for data and simulated signal events, after previous selec- tion requirements have been applied. . . . .	57
204			
205	Figure 28	The normalized, two-dimensional distribution of $E/p$ and $f_{\text{EM}}$ for simulated (a) $Z \rightarrow ee$ , (b) $Z \rightarrow \tau\tau$ , (c) 1200 GeV Stable R-Hadron events, and (d) 1200 GeV, 10 ns R-Hadron events. . . . .	58
206			
207	Figure 29	Two-dimensional distribution of $dE/dx$ versus charge signed momentum ( $qp$ ) for minimum-bias tracks. The fitted distributions of the most probable values for pi- ons, kaons and protons are superimposed. . . . .	59
208			
209			
210			
211			
212			
213			
214			
215			
216			
217			
218			
219			

220	Figure 30	The distribution of mass estimated using $dE/dx$ for simulated stable R-Hadrons with masses between 1000 and 1600 GeV. . . . .	60
221			
222			
223	Figure 31	The acceptance $\times$ efficiency as a function of R-Hadron (a) mass and (b) lifetime. (a) shows all of the combinations of mass and lifetime considered in this search, and (b) highlights the lifetime dependence for 1000 GeV and 1600 GeV R-Hadrons. . . . .	62
224			
225			
226			
227			
228	Figure 32	The distribution of (a) $dE/dx$ and (b) momentum for tracks in data and simulated signal after requiring the event level selection and the track selection on $p_T$ , hits, and $N_{\text{split}}$ . Each subfigure shows the normalized distributions for tracks classified as hadrons, electrons, and muons in data and R-Hadrons in the simulated signal. . . . .	64
229			
230			
231			
232			
233			
234			

235 LIST OF TABLES

247 LISTINGS

---

<small>248</small>	Listing 1	A floating example ( <code>listings</code> manual) . . . . .	80
--------------------	-----------	--	----

249 ACRONYMS

---

- 250 SM Standard Model  
251 LSP Lightest Supersymmetric Particle  
252 LHC Large Hadron Collider  
253 ToT time over threshold  
254 LCW local cluster weighted  
255 MIP minimally ionizing particle  
256 EPJC European Physical Journal C  
257 JES jet energy scale  
258 LLP Long-Lived Particle  
259 CR Control Region



260

## PART I

261

### INTRODUCTION

262

You can put some informational part preamble text here.



# 1

263

264 INTRODUCTION

---



265

## PART II

266

### THEORETICAL CONTEXT

267

You can put some informational part preamble text here.



# 2

268

## 269 STANDARD MODEL

---

270 The SM of particle physics seeks to explain the symmetries and interactions of  
271 all currently discovered fundamental particles. It has been tested by several genera-  
272 tions of experiments and has been remarkably successful, no significant de-  
273 viations have been found. The SM provides predictions in particle physics for  
274 interactions up to the Planck scale ( $10^{15}$ - $10^{19}$  GeV).

275 The theory itself is a quantum field theory grown from an underlying  $SU(3) \times$   
276  $SU(2) \times U(1)$  that requires the particle content and quantum numbers consist-  
277 ent with experimental observations (see Section 2.1). Each postulated symme-  
278 try is accompanied by an interaction between particles through gauge invari-  
279 ance. These interactions are referred to as the Strong, Weak, and Electromag-  
280 netic forces, which are discussed in Section 2.2.

281 Although this model has been very predictive, the theory is incomplete; for  
282 example, it is not able to describe gravity or astronomically observed dark matter.  
283 These limitations are discussed in more detail in Section 2.3.

## 284 21 PARTICLES

285 The most familiar matter in the universe is made up of protons, neutrons, and  
286 electrons. Protons and neutrons are composite particles, however, and are made  
287 up in turn by particles called quarks. Quarks carry both electric charge and color  
288 charge, and are bound in color-neutral combinations called baryons. The elec-  
289 tron is an example of a lepton, and carries only electric charge. Another type  
290 of particle, the neutrino, does not form atomic structures in the same way that  
291 quarks and leptons do because it carries no color or electric charge. Collectively,  
292 these types of particles are known as fermions, the group of particles with half-  
293 integer spin.

294 There are three generations of fermions, although familiar matter is formed  
295 predominantly by the first generation. The generations are identical except for  
296 their masses, which increase in each generation by convention. In addition, each  
297 of these particles is accompanied by an antiparticle, with opposite-sign quantum  
298 numbers but the same mass.

299 The fermions comprise what is typically considered matter, but there are  
300 additional particles that are mediators of interactions between those fermions.  
301 These mediators are known as the gauge bosons, gauge in that their existence  
302 is required by gauge invariance (discussed further in Section 2.2) and bosons in  
303 that they have integer spin. The boson which mediates the electromagnetic force  
304 is the photon, the first boson to be discovered; it has no electric charge, no mass,  
305 and a spin of 1. There are three spin-1 mediators of the weak force, the two  
306 W bosons and the Z boson. The W bosons have electric charge of  $\pm 1$  and a  
307 mass of  $80.385 \pm 0.015$  GeV, while the Z boson is neutral and has a mass of

308     $91.1876 \pm 0.0021$  GeV. The strong force is mediated by eight particles called  
 309    gluons, which are massless and electrically neutral but do carry color charge.

310    The final particle present in the SM is the Higgs boson, which was recently  
 311    observed for the first time by experiments at CERN in 2012. It is electrically  
 312    neutral, has a mass of  $125.7 \pm 0.4$  GeV, and is the only spin-0 particle yet to be  
 313    observed. The Higgs boson is the gauge boson associated with the mechanism  
 314    that gives a mass to the W and Z bosons.

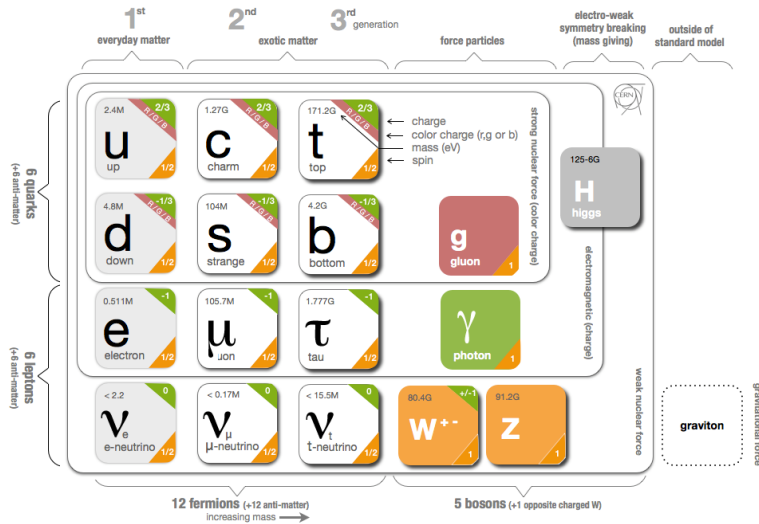


Figure 1: The particle content of the SM.

315    Together these particles form the entire content of the SM, and are summa-  
 316    rized in Figure 1. These are the particles that constitute the observable universe  
 317    and all the so-far-observed interactions within it.

## 318    2.2 INTERACTIONS

319    The interactions predicted and described by the SM are fundamentally tied to the  
 320    particles within it, both in that they describe the way those particles can influence  
 321    each other and also in that the existence of the interactions requires the existence  
 322    of some particles (the gauge bosons).

## 323    2.3 LIMITATIONS

# 3

324

325 SUPERSYMMETRY

---

326 3.1 MOTIVATION

327 3.2 STRUCTURE

328 3.3 PHENOMENOLOGY



# 4

329

330 LONG-LIVED PARTICLES

---

331 4.1 MECHANISMS

332 4.1.1 EXAMPLES IN SUPERSYMMETRY

333 4.2 PHENOMENOLOGY

334 4.2.1 DISIMILARITIES TO PROMPT DECAYS

335 4.2.2 CHARACTERISTIC SIGNATURES



336

### PART III

337

## EXPERIMENTAL STRUCTURE AND RECONSTRUCTION

338

You can put some informational part preamble text here.



# 5

339

340 THE LARGE HADRON COLLIDER

---

341 5.1 INJECTION CHAIN

342 5.2 DESIGN AND PARAMETERS

343 5.3 LUMINOSITY



# 6

344

## 345 THE ATLAS DETECTOR

---

346 6.1 COORDINATE SYSTEM

347 6.2 MAGNETIC FIELD

348 6.3 INNER DETECTOR

349 6.3.1 PIXEL DETECTOR

350 6.3.2 SEMICONDUCTOR TRACKER

351 6.3.3 TRANSITION RADIATION TRACKER

352 6.4 CALORIMETRY

353 6.4.1 ELECTROMAGNETIC CALORIMETERS

354 6.4.2 HADRONIC CALORIMETERS

355 6.4.3 FORWARD CALORIMETERS

356 6.5 MUON SPECTROMETER

357 6.6 TRIGGER

358 6.6.1 TRIGGER SCHEME

359 6.6.2 MISSING TRANSVERSE ENERGY TRIGGERS



# 7

360

## 361 EVENT RECONSTRUCTION

---

362 The ATLAS experiment combines measurements in the subdetectors to form a  
363 cohesive picture of each physics event.

## 364 7.1 TRACKS AND VERTICES

### 365 7.1.1 TRACK RECONSTRUCTION

#### 366 7.1.1.1 NEURAL NETWORK

#### 367 7.1.1.2 PIXEL DE/DX

#### 368 7.1.2 VERTEX RECONSTRUCTION

## 369 7.2 JETS

### 370 7.2.1 TOPOLOGICAL CLUSTERING

### 371 7.2.2 JET ENERGY SCALE

### 372 7.2.3 JET ENERGY SCALE UNCERTAINTIES

### 373 7.2.4 JET ENERGY RESOLUTION

## 374 7.3 ELECTRONS

### 375 7.3.1 ELECTRON IDENTIFICATION

## 376 7.4 MUONS

### 377 7.4.1 MUON IDENTIFICATION

## 378 7.5 MISSING TRANSVERSE ENERGY



379

## PART IV

380

### CALORIMETER RESPONSE

381

You can put some informational part preamble text here.



384 As discussed in Section 7.2, colored particles produced in collisions hadronize  
385 into jets of multiple hadrons. One approach to understanding jet physics in the  
386 ATLAS calorimetry is to evaluate the calorimeter response to those individual  
387 hadrons; measurements of individual hadrons can be used to build up an under-  
388 standing of the jets that they form. The redundancy of the momentum provided  
389 by the tracking system and the energy provided by the calorimeter provides an  
390 opportunity to study calorimeter response using real collisions, as described fur-  
391 ther in Section 8.2.

392 Calorimeter response includes a number of physical effects that can be ex-  
393 tracted to provide insight into many aspects of jet modeling. First, many charged  
394 hadrons interact with the material of the detector prior to reaching the calorime-  
395 ters and thus do not deposit any energy. Comparing this effect in data and sim-  
396 ulation is a powerful tool in validating the interactions of particles with the ma-  
397 terial of the detector and the model of the detector geometry in simulation, see  
398 Section 8.2.2. The particles which do reach the calorimeter deposit their energy  
399 into individual cells, which are then clustered to measure full energy deposits.  
400 Comparing the response in data to simulated hadrons provides a direct evalua-  
401 tion of noise in the calorimeters, the showering of hadronic particles, and the  
402 energy deposited by particles in matter (Section 8.2.4). These measurements are  
403 extended to explore several additional effects, such as the dependence on charge,  
404 in Section 8.2.4.1.

405 The above studies all use an inclusive selection of charged particles, which are  
406 comprised predominantly of pions, kaons, and (anti)protons. It is also possible  
407 to measure the particle types separately to evaluate the simulated interactions of  
408 each particle, particularly at low energies where differences between species are  
409 very relevant. Pions and (anti)protons can be identified through decays of long-  
410 lived particles, in particular  $\Lambda$ ,  $\bar{\Lambda}$ , and  $K_S^0$ , and then used to measure response as  
411 described above. This is discussed in detail in Section 8.3.

412 Together, these measurements in data provide a thorough understanding of  
413 the way hadrons interact with the ATLAS detector and can be used to build up a  
414 description of jets, as seen in Chapter 9. The results in this chapter use data col-  
415 lected at 7 and 8 TeV collected in 2010 and 2012, respectively. Both are included  
416 as the calorimeter was repaired and recalibrated between those two data-taking  
417 periods. Both sets of data are compared to an updated simulation that includes  
418 new physics models provided by Geant4 [1] and improvements in the detec-  
419 tor description [2, 3]. These results are published in European Physical Journal  
420 C (EPJC) [4] and can be compared to a similar measurement performed in 2009  
421 and 2010 [5], which used the previous version of the simulation framework [6].

## 422 8.1 DATASET AND SIMULATION

## 423 8.1.1 DATA SAMPLES

424 The two datasets used in this chapter are taken from dedicated low-pileup runs  
 425 where the fraction of events with multiple interactions was negligible, to facilitate  
 426 measurement of isolated hadrons. The 2012 dataset at  $\sqrt{s} = 8$  TeV contains  
 427 8 million events and corresponds to an integrated luminosity of  $0.1 \text{ nb}^{-1}$ . The  
 428 2010 dataset at  $\sqrt{s} = 7$  TeV contains 3 million events and corresponds to an  
 429 integrated luminosity of  $3.2 \text{ nb}^{-1}$ . The latter dataset was also used in the 2010  
 430 results [5], but it has since been reanalyzed with an updated detector description  
 431 for the material and alignment.

## 432 8.1.2 SIMULATED SAMPLES

433 The two datasets above are compared to simulated single-, double-, and non-  
 434 diffractive events generated with Pythia8 [7] using the A2 configuration of  
 435 hadronization [8] and the MSTW 2008 parton-distribution function set [9, 10].  
 436 The conditions and energies for each run are matched in the two simulations.

437 To evaluate the interaction of hadrons with detector material, the simulation  
 438 uses two different collections of hadronic physics models, called physics lists, in  
 439 Geant4 9.4 [11]. The first, QGSP\_BERT, combines the Bertini intra-nuclear  
 440 cascade [12–14] below 9.9 GeV, a parametrized proton inelastic model from 9.5  
 441 to 25 GeV [15], and a quark-gluon string model above 12 GeV [16–20]. The  
 442 second, FTFP\_BERT, combines the Bertini intra-nuclear cascade [12–14] below  
 443 5 GeV and the Fritiof model [21–24] above 4 GeV. In either list, Geant4 en-  
 444 forces a smooth transition between models where multiple models overlap.

## 445 8.1.3 EVENT SELECTION

446 The event selection for this study is minimal, as the only requirement is selecting  
 447 good-quality events with an isolated track. Such events are triggered by requir-  
 448 ing at least two hits in the minimum-bias trigger scintillators. After trigger, each  
 449 event is required to have exactly one reconstructed vertex, and that vertex is re-  
 450 quired to have four or more associated tracks.

451 The particles which enter into the response measurements are first identified  
 452 as tracks in the inner detector. The tracks are required to have at least 500 MeV  
 453 of transverse momentum. To ensure a reliable momentum measurement, these  
 454 tracks are required to have at least one hit in the pixel detector, six hits in the SCT,  
 455 and small longitudinal and transverse impact parameters with respect to the pri-  
 456 mary vertex [5]. For the majority of the measurements in this chapter, the track is  
 457 additionally required to have 20 hits in the TRT, which significantly reduces the  
 458 contribution from tracks which undergo nuclear interactions. This requirement  
 459 and its effect is discussed in more detail in Section 8.2.4.1. In addition, tracks are  
 460 rejected if there is another track which extrapolates to the calorimeter within a

cone of  $\Delta R = \sqrt{(\Delta\phi)^2 + (\Delta\eta)^2} < 0.4$ . This requirement guarantees that the contamination of energy from nearby charged particles is negligible [5].

## 8.2 INCLUSIVE HADRON RESPONSE

The calorimeter response is more precisely defined as the ratio of the measured calorimeter energy to the true energy carried by the particle, although this true energy is unknown. For charged particles, however, the inner detector provides a very precise measurement of momentum (with uncertainty less than 1%) that can be used as a proxy for true energy. The ratio of the energy deposited by the charged particle in the calorimeter,  $E$ , to its momentum measured in the inner detector  $p$ , forms the calorimeter response measure called  $E/p$ . Though the distribution of  $E/p$  contains a number of physical features, this study focuses on the trends in two aggregated quantities:  $\langle E/p \rangle$ , the average of  $E/p$  within a given subset of particles, and the zero fraction, the fraction of particles with no associated energy in the calorimeter.

The calorimeter energy assigned to a track particle is defined using clusters. The clusters are formed using a 4–2–0 algorithm [25] that begins with seeds requiring at least 4 times the average calorimeter noise. The neighboring cells with at least twice that noise threshold are then added to the cluster, and all bounding cells are then added with no requirement. This algorithm minimizes noise contributions through its seeding process, and including the additional layers improves the energy resolution [26]. The clusters are associated to a given track if they fall within a cone of  $\Delta R = 0.2$  of the extrapolated position of the track, which includes about 90% of the energy on average [5]. This construction is illustrated in Figure 2.

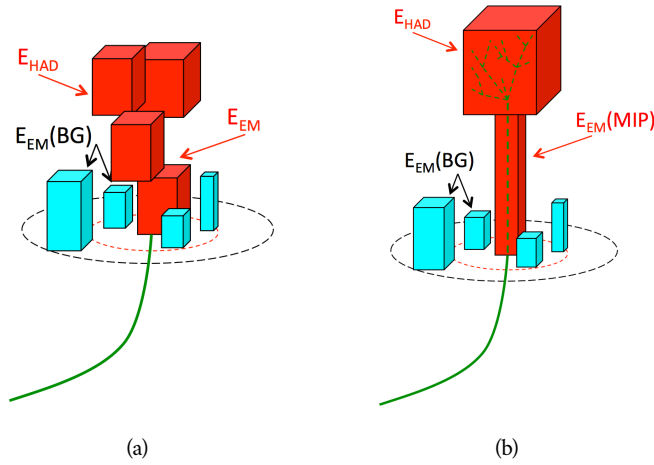


Figure 2: An illustration (a) of the  $E/p$  variable used throughout this paper. The red energy deposits come from the charged particle targeted for measurement, while the blue energy deposits are from nearby neutral particles and must be subtracted. The same diagram (b) for the neutral-background selection, described in Section 8.2.3.

## 485 8.2.1 E/P DISTRIBUTION

486 The  $E/p$  distributions measured in both data and simulation are shown in Figure 3 for two example bins of track momentum and for tracks in the central  
 487 region of the detector. These distributions show several important features of  
 488 the  $E/p$  observable. The large content in the bin at  $E = 0$  comes from tracks  
 489 that have no associated cluster, which occurs due to interactions with detector  
 490 material prior to reaching the calorimeter or the energy deposit being insuffi-  
 491 ciently large to generate a seed, and are discussed in Section 8.2.2. The small  
 492 negative tail comes from similar tracks that do not deposit any energy in the  
 493 calorimeter but are randomly associated to a noise cluster. The long positive  
 494 tail above 1.0 comes from the contribution of neutral particles. Nearby neutral  
 495 particles deposit (sometimes large) additional energy in the calorimeter but do  
 496 not produce tracks in the inner detector, so they cannot be rejected by the track  
 497 isolation requirement. Additionally the peak and mean of the distribution falls  
 498 below 1.0 because of the loss of energy not found within the cone as well as the  
 499 non-compensation of the calorimeter.  
 500

501 The data and simulation share the same features, but the high and low tails  
 502 are significantly different. The simulated events tend to overestimate the con-  
 503 tribution of neutral particles to the long tail, an effect which can be isolated and  
 504 removed as discussed in Section 8.2.3. Additionally, the simulated clusters have  
 505 less noise on average, although this is a small effect on the overall response.

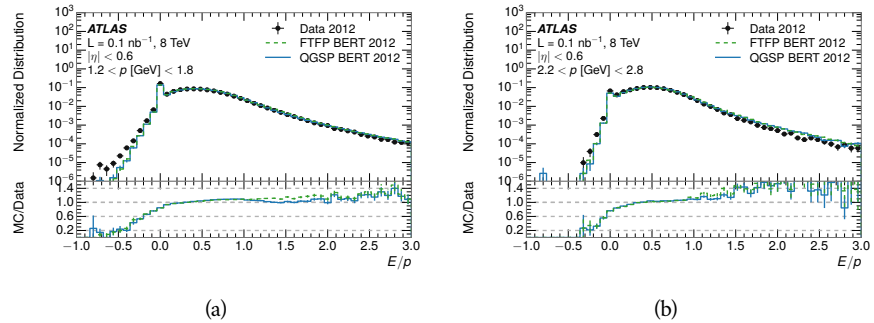


Figure 3: The  $E/p$  distribution and ratio of simulation to data for isolated tracks with  
 (a)  $|\eta| < 0.6$  and  $1.2 < p/\text{GeV} < 1.8$  and (b)  $|\eta| < 0.6$  and  $2.2 < p/\text{GeV} < 2.8$ .

## 506 8.2.2 ZERO FRACTION

507 The fraction of particles with no associated clusters, or similarly those with  $E \leq$   
 508 0, reflects the modeling of both the detector geometry and hadronic interactions.  
 509 The zero fraction is expected to rise as the amount of material a particle traverses  
 510 increases, while it is expected to decrease as the particle energy increases. This  
 511 dependence can be seen in Figure 4, where the zero fraction in data and simula-  
 512 tion is shown as a function of momentum and the amount of material measured  
 513 in interaction lengths. The trends are similar between the 2010 and 2012 mea-  
 514 surements. The zero fraction decreases with energy as expected. The amount of

material in the detector increases with  $\eta$ , which provides a distribution of interaction lengths. As the data and simulation have significant disagreement in the zero fraction over a number of interaction lengths, the difference must be primarily from the modeling of hadronic interactions with detector material and not just the detector geometry.

There is also a noticeable difference between positive and negative tracks at low momentum, which reflects the difference in response between protons and antiprotons. Antiprotons have significant model differences in the two physics lists, QGSP\_BERT and FTFP\_BERT, and this is evident in the lowest momentum bin of the data to simulation ratio. This difference is explored further in Section 8.3.

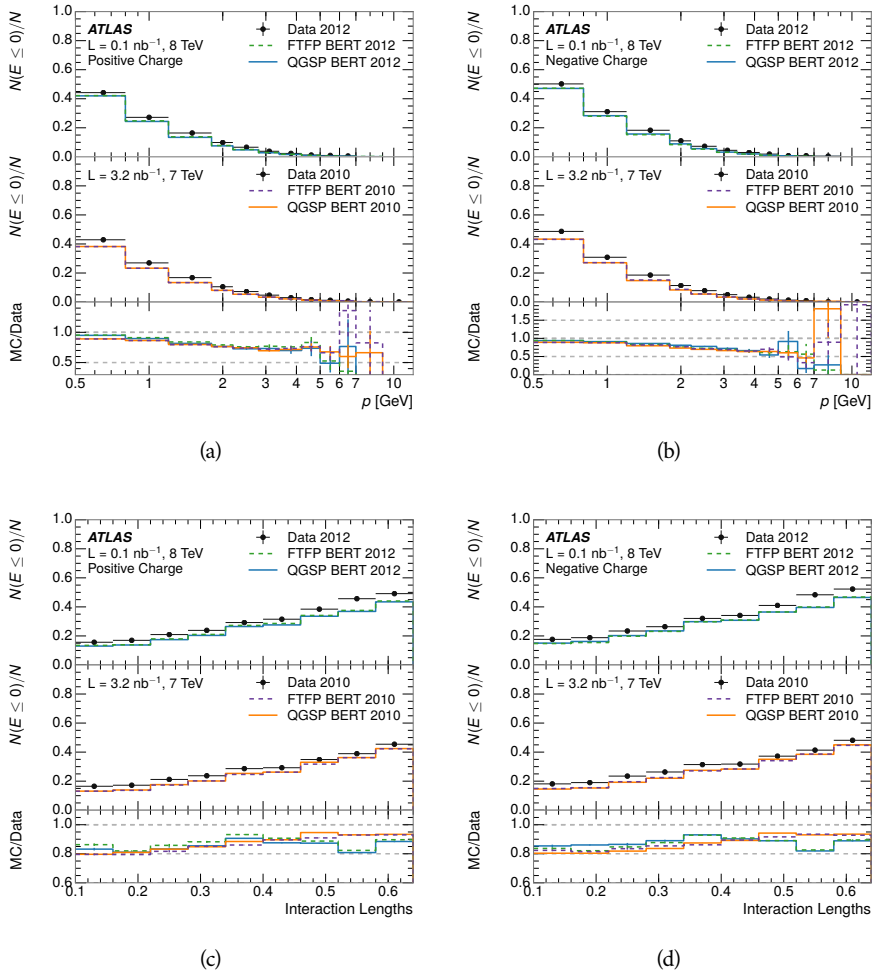


Figure 4: The fraction of tracks as a function (a, b) of momentum, (c, d) of interaction lengths with  $E \leq 0$  for tracks with positive (on the left) and negative (on the right) charge.

## 526 8.2.3 NEUTRAL BACKGROUND SUBTRACTION

527 The isolation requirement on hadrons is only effective in remove energy contri-  
 528 bution from nearby charged particles. Nearby neutral particles, predominantly  
 529 photons from  $\pi^0$  decays, also add their energy to the calorimeter clusters, but  
 530 mostly in the electromagnetic calorimeter. It is possible to measure this contri-  
 531 bution, on average, using late-showering hadrons that minimally ionize in the  
 532 electromagnetic calorimeter. Such particles are selected by requiring that they  
 533 deposit less than 1.1 GeV in the EM calorimeter within a cone of  $\Delta R < 0.1$   
 534 around the track. To ensure that these particles are well measured, they are addi-  
 535 tionally required to deposit between 40% and 90% of their energy in the hadronic  
 536 calorimeter within the same cone.

537 These particles provide a clean sample to measure the nearby neutral back-  
 538 ground because they do not deposit energy in the area immediately surrounding  
 539 them in the EM calorimeter, as shown in Figure 2. So, the energy deposits in the  
 540 region  $0.1 < \Delta R < 0.2$  can be attributed to neutral particles alone. To estimate  
 541 the contribution to the whole cone considered for the response measurement,  
 542 that energy is scaled by a geometric factor of 4/3. This quantity,  $\langle E/p \rangle_{\text{BG}}$ , mea-  
 543 sured in aggregate over a number of particles, gives the contribution to  $\langle E/p \rangle$   
 544 from neutral particles in the EM calorimeter. Similar techniques were used in  
 545 the individual layers of the hadronic calorimeters to show that the background  
 546 from neutrals is negligible in those layers [5].

547 The distribution of this background estimate is shown in Figure 5. Although  
 548 the simulation captures the overall trend, it significantly overestimates the neu-  
 549 tral contribution for tracks with momentum between 2 and 8 GeV. This effect  
 550 was also seen in the tails of the  $E/p$  distributions in Figure 3. This difference is  
 551 likely due to the modeling of coherent neutral particle radiation in Pythia8, as  
 552 the discrepancy does not depend on  $\eta$  and thus is unlikely to be a mismodeling  
 553 of the detector. This difference can be subtracted to form a corrected average  
 554  $E/p$ , as in Section 8.2.4.

## 555 8.2.4 CORRECTED RESPONSE

556 Figure 6 shows  $\langle E/p \rangle_{\text{COR}}$  as a function of momentum for several bins of pseu-  
 557 dorapidity. This corrected  $\langle E/p \rangle_{\text{COR}} \equiv \langle E/p \rangle - \langle E/p \rangle_{\text{BG}}$  measures the average  
 558 calorimeter response without the contamination of neutral particles. It is the  
 559 most direct measurement of calorimeter response in that it is the energy mea-  
 560 sured for fully isolated hadrons. The correction is performed separately in data  
 561 and simulation, so that the mismodeling of the neutral background in simulation  
 562 is removed from the comparison of response. The simulation overestimates the  
 563 response at low momentum by about 5%, an effect that can be mostly attributed  
 564 to the underestimation of the zero fraction mentioned previously.

565 The response measurement above used topological clustering at the EM scale,  
 566 that is clusters were formed to measure energy but no corrections were applied  
 567 to correct for expected effects like energy lost outside of the cluster or in unin-  
 568 strumented material. It is also interesting to measure  $\langle E/p \rangle_{\text{COR}}$  using local clus-

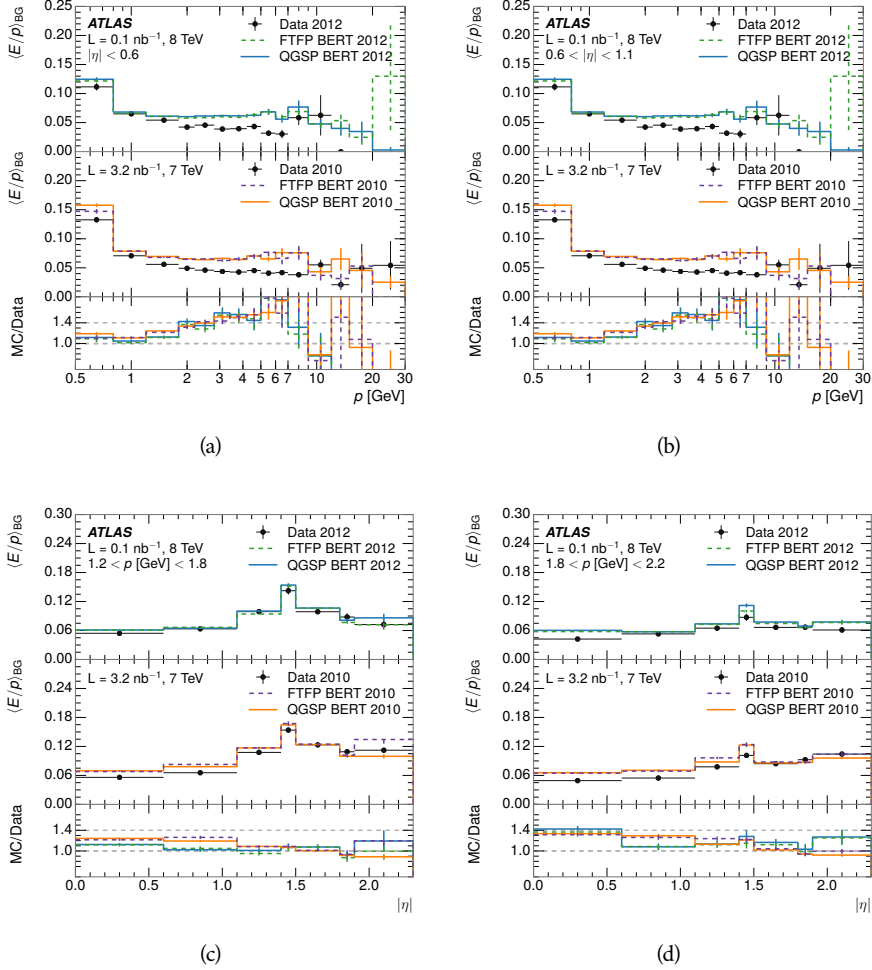


Figure 5:  $\langle E/p \rangle_{\text{BG}}$  as a function of the track momentum for tracks with (a)  $|\eta| < 0.6$ , (b)  $0.6 < |\eta| < 1.1$ , and as a function of the track pseudorapidity for tracks with (c)  $1.2 < p/\text{GeV} < 1.8$ , (d)  $1.8 < p/\text{GeV} < 2.2$ .

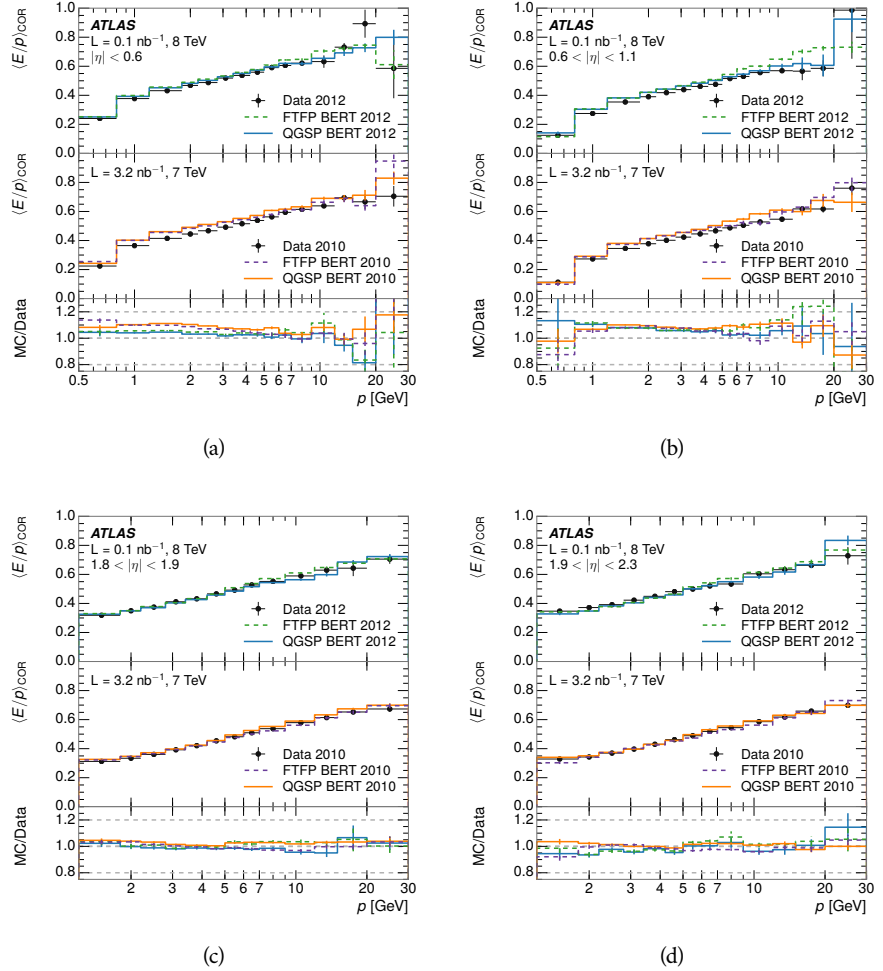


Figure 6:  $\langle E/p \rangle_{\text{COR}}$  as a function of track momentum, for tracks with (a)  $|\eta| < 0.6$ , (b)  $0.6 < |\eta| < 1.1$ , (c)  $1.8 < |\eta| < 1.9$ , and (d)  $1.9 < |\eta| < 2.3$ .

569 ter weighted (LCW) energies, which accounts for those effects by calibrating the  
 570 energy based on the properties of the cluster such as energy density and depth in  
 571 the calorimeter. Figure 7 shows these distributions for tracks with zero or more  
 572 clusters and separately for tracks with one or more clusters. The calibration  
 573 moves  $\langle E/p \rangle_{\text{COR}}$  significantly closer to 1.0, which is the purpose of the calibra-  
 574 tion. The agreement between data and simulation improves noticeably when at  
 575 least one cluster is required, as this removes the contribution from the mismod-  
 576 eling of the zero fraction.

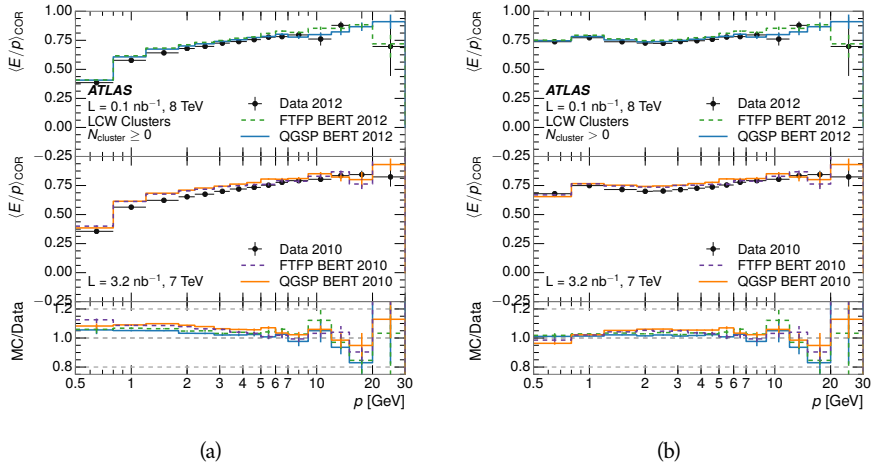


Figure 7:  $\langle E/p \rangle_{\text{COR}}$  calculated using LCW-calibrated topological clusters as a function of track momentum for tracks with (a) zero or more associated topological clusters or (b) one or more associated topological clusters.

#### 577 8.2.41 ADDITIONAL STUDIES

578 As has been seen in several previous measurements, the simulation does not  
 579 correctly model the chance of a low momentum hadron to reach the calorime-  
 580 ter. Because of the consistent discrepancy across pseudorapidity and interaction  
 581 lengths, this seems to be best explained by incomplete understanding of hadronic  
 582 interactions with the detector. For example, a hadron that scatters off of a nu-  
 583 cleus in the inner detector can be deflected through a significant angle and not  
 584 reach the expected location in the calorimeter. In addition, these interactions  
 585 can produce secondary particles that are difficult to model.

586 The requirement on the number of hits in the TRT reduces these effects by  
 587 preferentially selecting tracks that do not undergo nuclear interactions. It is inter-  
 588 esting to check how well the simulation models tracks with low numbers of  
 589 TRT hits, where the nuclear interactions are much more likely. Figure 8 com-  
 590 pares the distributions with  $N_{\text{TRT}} < 20$  to  $N_{\text{TRT}} > 20$  for real and simulated  
 591 particles. As expected, the tracks with fewer hits are poorly modeled in the sim-  
 592 ulation as  $\langle E/p \rangle_{\text{COR}}$  differs by as much as 25% at low momentum.

593 Another interesting aspect of the simulation is the description of antiprotons  
 594 at low momentum, where QGSP\_BERT and FTFP\_BERT have significant differ-  
 595 ences. This can be seen to have an effect in the inclusive response measurement

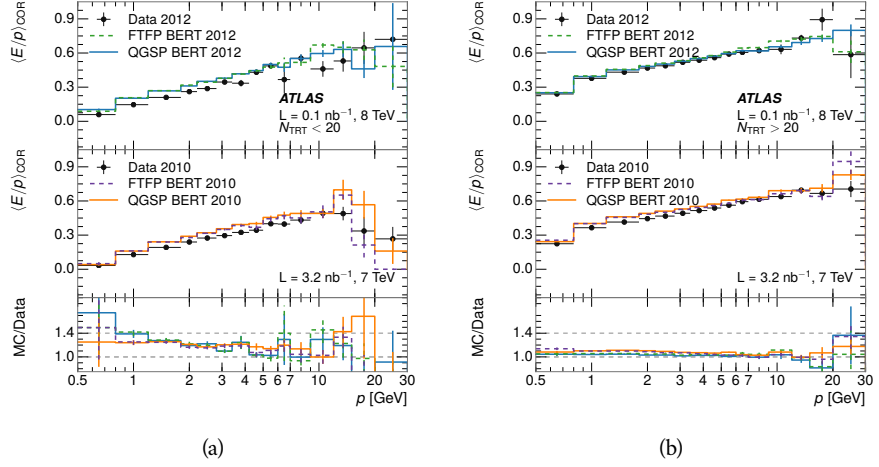


Figure 8: Comparison of the  $\langle E/p \rangle_{\text{COR}}$  for tracks with (a) less than and (b) greater than 20 hits in the TRT.

when separated into positive and negative charge. The  $\langle E/p \rangle_{\text{COR}}$  distributions for positive and negative particles are shown in Figure 9, where a small difference between QGSP\_BERT and FTFP\_BERT can be seen in the distribution for negative tracks. This is demonstrated more clearly in Figure 10, which shows the  $E/p$  distribution in the two simulations separated by charge. There is a clear difference around  $E/p > 1.0$ , which can be explained by the additional energy deposited by the annihilation of the antiproton in the calorimeter that is modeled well only in FTFP\_BERT. This is also explored with data using identified antiprotons in Section 8.3.

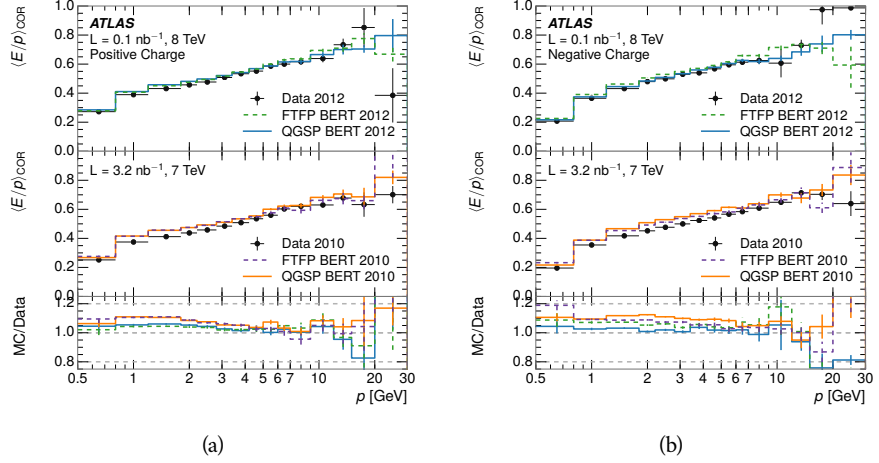


Figure 9: Comparison of the  $\langle E/p \rangle_{\text{COR}}$  for (a) positive and (b) negative tracks as a function of track momentum for tracks with  $|\eta| < 0.6$ .

The  $\langle E/p \rangle$  results in previous sections have considered the electromagnetic and hadronic calorimeters together as a single energy measurement, to emphasize the total energy deposited for a given particle. However, the deposits in each

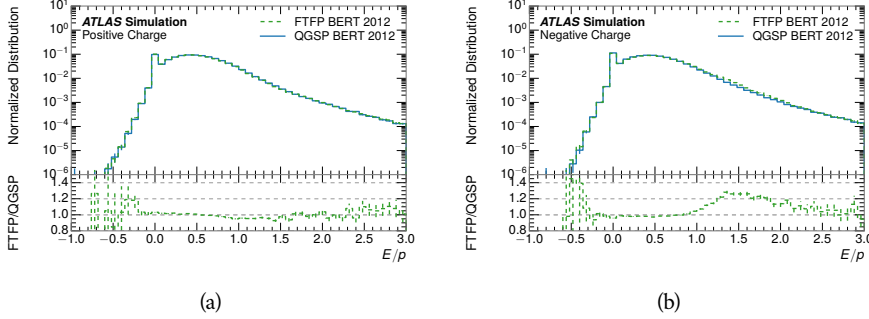


Figure 10: Comparison of the  $E/p$  distributions for (a) positive and (b) negative tracks with  $0.8 < p/\text{GeV} < 1.2$  and  $|\eta| < 0.6$ , in simulation with the FTFP\_BERT and QGSP\_BERT physics lists.

calorimeter are available separately and  $\langle E/p \rangle$  can be constructed for each layer. As the layers are composed of different materials and are modeled separately in the detector geometry, confirmation that the simulation matches the data well in each layer adds confidence in both the description of hadronic interactions with the two different materials and also the geometric description of each.

The technique discussed in Section 8.2.3 for selecting minimally ionizing particle (**MIP**s) in the electromagnetic calorimeter is also useful in studying deposits in the hadronic calorimeter. Those **MIP**s deposit almost all of their energy exclusively in the hadronic calorimeter. Figure 11 shows  $\langle E/p \rangle_{\text{Had}}^{\text{Had}}$ , where RAW indicates that no correction has been applied for neutral backgrounds and Had indicates that only clusters for the hadronic calorimeter are included. The RAW and COR versions of  $\langle E/p \rangle$  in this case are the same, as the neutral background is negligible in that calorimeter layer. The distributions are shown both for the original EM scale calibration and after LCW calibration. The data and simulation agree very well in this comparison, except in the lowest momentum bin which has 5% discrepancy that has already been seen in similar measurements.

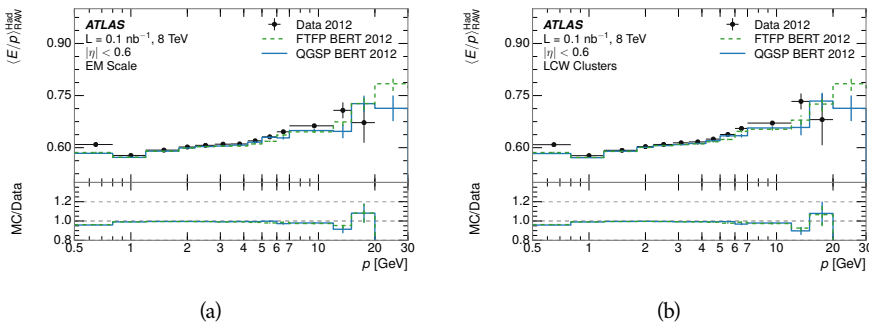


Figure 11: Comparison of the response of the hadronic calorimeter as a function of track momentum (a) at the EM-scale and (b) after the LCW calibration.

A similar comparison can be made in the electromagnetic calorimeter by selecting particles which have no associated energy in the hadronic calorimeter. These results are measured in terms of  $\langle E/p \rangle_{\text{COR}}^{\text{EM}}$ , where EM designates that

627 only clusters in the electromagnetic calorimeter are included and COR designates  
 628 that the neutral background is subtracted as the neutral background is  
 629 present in this case. Figure 12 shows the analogous comparisons to Figure 11 in  
 630 the electromagnetic calorimeter. In this case the disagreement between data and  
 631 simulation is more pronounced, with discrepancies as high as 5% over a larger  
 632 range of momenta. This level of discrepancy indicates that the description of  
 633 the electromagnetic calorimeter is actually the dominant source of discrepancy  
 634 in the combined distributions in Section 8.2.4.

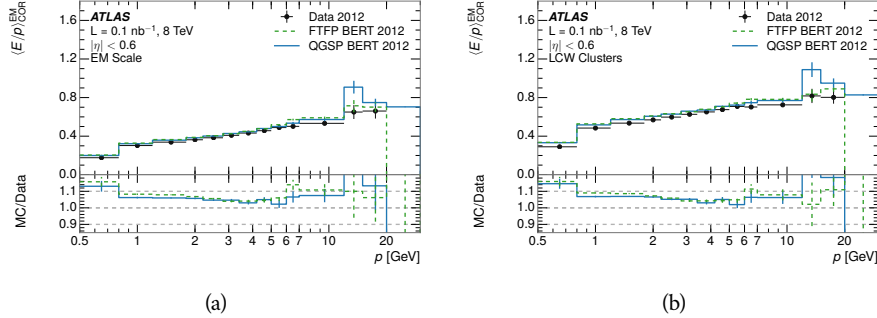


Figure 12: Comparison of the response of the EM calorimeter as a function of track momentum (a) at the EM-scale and (b) with the LCW calibration.

635 **NOTE: There are more studies that I skipped for brevity that could be in-**  
 636 **cluded if interesting. E/p at different cluster threshold settings, E/p with**  
 637 **pileup, E/p with cells. I also left out a lot of eta bins that appear in the**  
 638 **paper so that this section didn't turn into 20 pages of plots.**

### 639 8.3 IDENTIFIED PARTICLE RESPONSE

640 The inclusive response measurement for hadrons can be augmented by measur-  
 641 ing the response for specific particle species. The simulation models each parti-  
 642 cle type separately, and understanding the properties of each is important in con-  
 643 straining the uncertainty on jets. In order to select and measure specific hadrons,  
 644 this section relies on the displaced decays of long-lived particles. Such decays  
 645 can be identified by reconstructing secondary vertices with a requirement on  
 646 mass. In particular,  $\Lambda$ ,  $\bar{\Lambda}$ , and  $K_S^0$  can be used to select a pure sample of protons,  
 647 antiprotons, and pions, respectively.

#### 648 8.3.1 DECAY RECONSTRUCTION

649 The measurement of response for identified particles uses the same selection as  
 650 for inclusive particles (Section 8.1.3) with a few additions. Each event used is  
 651 required to have at least one secondary vertex, and the tracks are required to  
 652 match to that vertex rather than the primary vertex. Pions are selected from  
 653 decays of  $K_S^0 \rightarrow \pi^+ \pi^-$ , which is the dominant decay for  $K_S^0$  to charged particles.  
 654 Protons are selected from decays of  $\Lambda \rightarrow \pi^- p$  and antiprotons from  $\bar{\Lambda} \rightarrow \pi^+ \bar{p}$ ,

which are similarly the dominant decays of  $\Lambda$  and  $\bar{\Lambda}$  to charged particles. The species of parent hadron in these decays is determined by reconstructing the mass of the tracks associated to the secondary vertex. The sign of the higher momentum decay particle can distinguish between  $\Lambda$  and  $\bar{\Lambda}$ , which of course have the same mass, as the proton or antiproton is kinematically favored to have higher momentum. Examples of the reconstructed masses used to select these decays are shown in Figure 13.

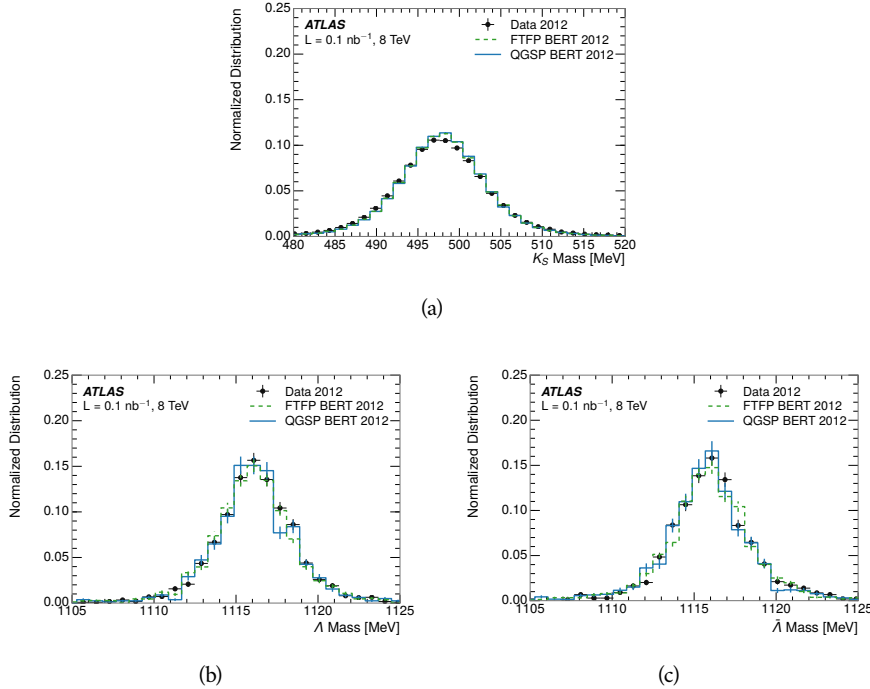


Figure 13: The reconstructed mass peaks of (a)  $K_S^0$ , (b)  $\Lambda$ , and (c)  $\bar{\Lambda}$  candidates.

The dominant backgrounds for the identified particle decays are nuclear interactions and combinatoric sources. These are suppressed by the kinematic requirements on the tracks as well as an additional veto which removes candidates that are consistent with both a  $\Lambda$  or  $\bar{\Lambda}$  and a  $K_S^0$  hypothesis, which is possible because of the different assumptions on particle mass in each case [5]. After these requirements, the backgrounds are found to be negligible compared to the statistical errors on these measurements.

### 8.3.2 IDENTIFIED RESPONSE

With these techniques the  $E/p$  distributions are extracted in data and simulation for each particle species and shown in Figure 14. These distributions are shown for a particular bin of  $E_a$  ( $2.2 < E_a/\text{GeV} < 2.8$ ), rather than  $p$ .  $E_a$  is the energy available to be deposited in the calorimeter: for pions  $E_a = \sqrt{p^2 + m^2}$ , for protons  $E_a = \sqrt{p^2 + m^2} - m$ , and for antiprotons  $E_a = \sqrt{p^2 + m^2} + m$ . The features of the  $E/p$  distributions are similar to the inclusive case. There is a small negative tail from noise and a large fraction of tracks with zero energy from particles which do not reach the calorimeter. The long positive tail is noticeably more

678 pronounced for antiprotons because of the additional energy generated by the  
 679 annihilation in addition to the neutral background.

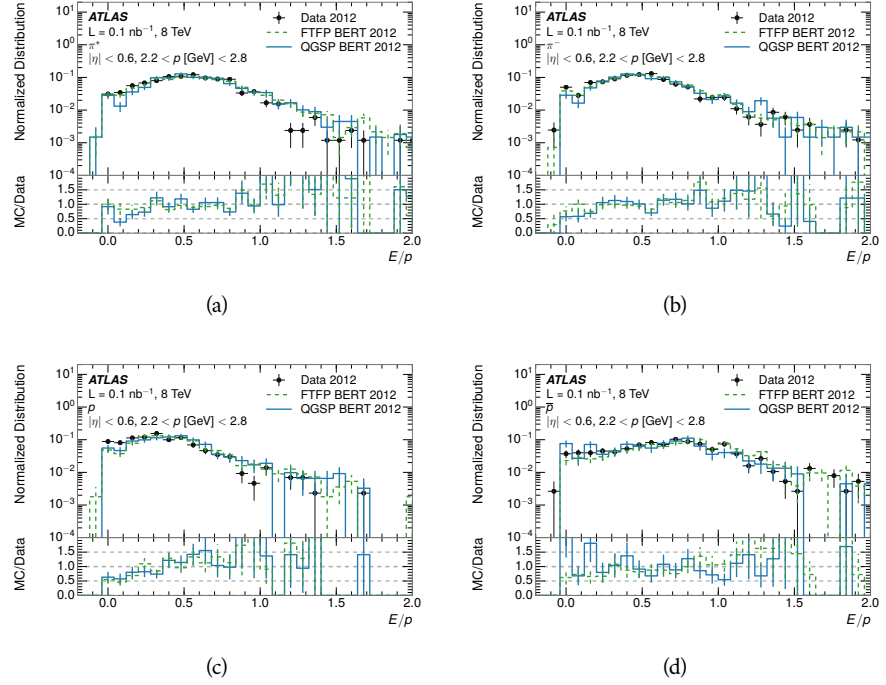


Figure 14: The  $E/p$  distribution for isolated (a)  $\pi^+$ , (b)  $\pi^-$ , (c) proton, and (d) anti-proton tracks.

680 The zero fraction is further explored in Figure 15 for pions and protons in data  
 681 and simulation. The simulation consistently underestimates the zero fraction  
 682 independent of particle species, which implies that this discrepancy is not caused  
 683 by the model of a particular species but rather a feature common to all.

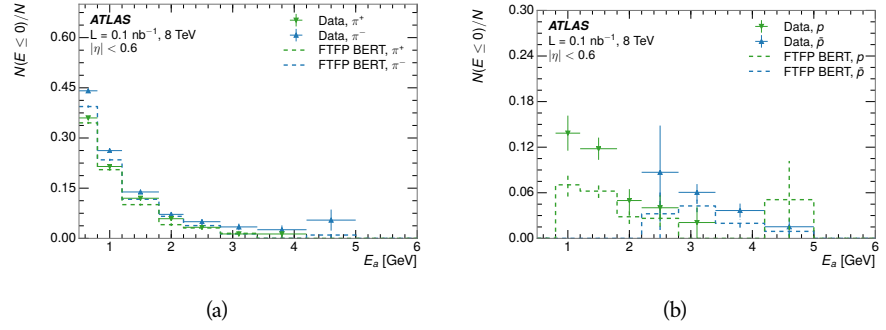


Figure 15: The fraction of tracks with  $E \leq 0$  for identified (a)  $\pi^+$  and  $\pi^-$ , and (b) proton and anti-proton tracks

684 It is also interesting to compare the response between the different particle  
 685 species. One approach to do this is to measure the difference in  $\langle E/p \rangle$  between  
 686 two types, which has the advantage of removing the neutral background. These  
 687 differences are shown in various combinations in Figure 16. The response for

688  $\pi^+$  is greater on average than the response to  $\pi^-$  because of a charge-exchange  
 689 effect which causes the production of additional neutral pions in the showers of  
 690  $\pi^+$  [27]. The response for  $\pi^+$  is also greater on average than the response to  $p$ ,  
 691 because a large fraction of the energy of  $\pi^+$  hadrons is converted to an electro-  
 692 magnetic shower [28, 29]. However, the  $\bar{p}$  response is significantly higher than  
 693 the response to  $\pi^-$  because of the annihilation of the antiproton. FTFP\_BERT  
 694 does a better job of modeling this effect than QGSP\_BERT because of their differ-  
 695 ent descriptions of  $\bar{p}$  interactions with material.

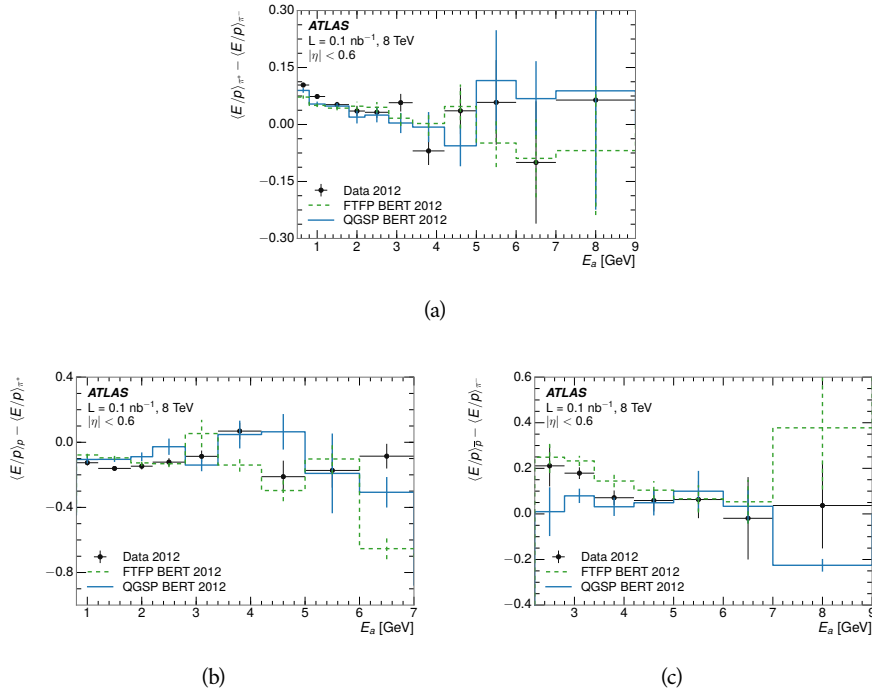


Figure 16: The difference in  $\langle E/p \rangle$  between (a)  $\pi^+$  and  $\pi^-$  (b)  $p$  and  $\pi^+$ , and (c)  $\bar{p}$  and  $\pi^-$ .

696 It is also possible to remove the neutral background from these response dis-  
 697 tributions using the same technique as in Section 8.2.3. The technique is largely  
 698 independent of the particle species and so can be directly applied to  $\langle E/p \rangle$  for  
 699 pions. The  $\langle E/p \rangle_{\text{COR}}$  distributions for pions are shown in Figure 17, which are  
 700 very similar to the inclusive results. The inclusive hadrons are comprised mostly  
 701 of pions, so this similarity is not surprising. It is also possible to see the small  
 702 differences between  $\pi^+$  and  $\pi^-$  response here, where  $\langle E/p \rangle_{\text{COR}}$  is higher on av-  
 703 erage for  $\pi^+$ . The agreement between data and simulation is significantly worse  
 704 for the  $\pi^-$  distributions than for the  $\pi^+$ , with a discrepancy greater than 10%  
 705 below 2-3 GeV.

### 706 8.3.3 ADDITIONAL SPECIES IN SIMULATION

707 The techniques above provide a method to measure the response separately for  
 708 only pions and protons. However the hadrons which forms jets include a num-  
 709 ber of additional species such as kaons and neutrons. The charged kaons are

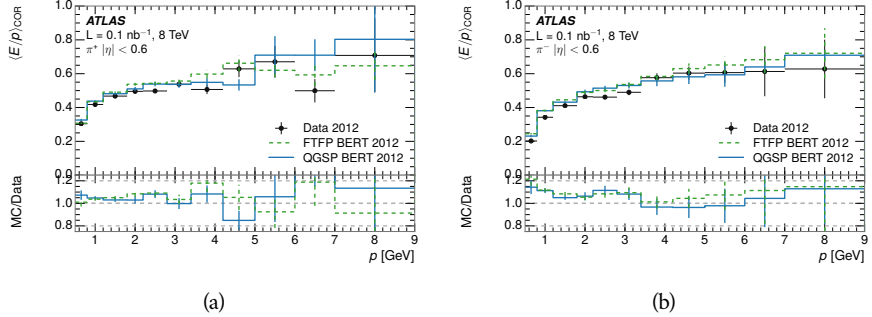


Figure 17:  $\langle E/p \rangle_{\text{COR}}$  as a function of track momentum for (a)  $\pi^+$  tracks and (b)  $\pi^-$  tracks.

an important component of the inclusive charged hadron distribution, which is comprised of roughly 60-70% pions, 15-20% kaons, and 5-15% protons. These are difficult to measure in data at the ATLAS detector, although a template subtraction technique has been proposed which may be effective with larger sample sizes [4]. The simulation of these particles includes noticeable differences in response at low energies, which are shown in Figure 18 for FTFP\_BERT. The significant differences in response between low energy protons and antiprotons are accounted for above in the definitions of  $E_a$ .

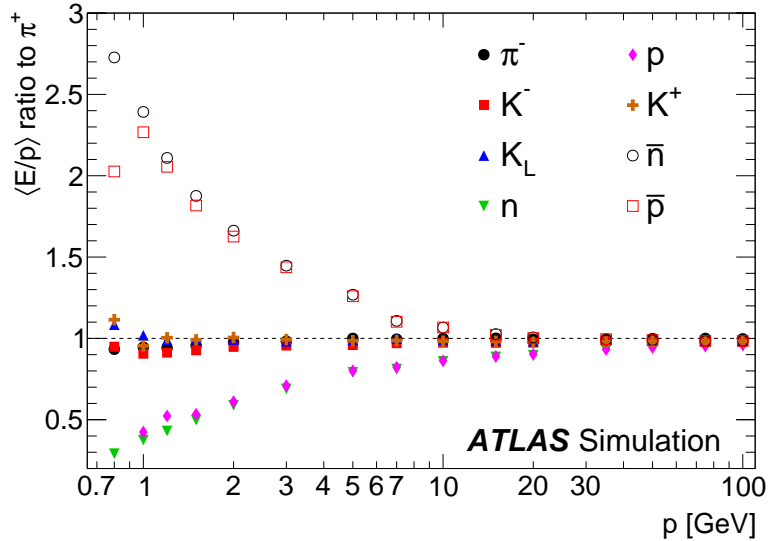


Figure 18: The ratio of the calorimeter response to single particles of various species to the calorimeter response to  $\pi^+$  with the physics list FTFP\_BERT.

#### 8.4 SUMMARY

These various measurements of calorimeter response shown above for data and simulation illuminate the accuracy of the simulation of hadronic interactions at the ATLAS detector. The results were done using 2010 and 2012 data at 7 and 8

722 TeV, but reflect the most current understanding of the detector alignment and  
723 geometry. A number of measurements focusing on a comparison between pro-  
724 tons and antiprotons suggest that FTFP\_BERT models those interaction more  
725 accurately than QGSP\_BERT. These measurements, among others, were the moti-  
726 vation to switch the default Geant4 simulation from FTFP\_BERT to QGSP\_BERT  
727 for all ATLAS samples.

728 Even with these updates, there are a number of small, approximately 5%, dis-  
729 crepancies in response between the data and simulation at low energies. At  
730 higher energies the simulation of hadronic interactions is very consistent with  
731 data. Chapter 9 discusses how to use these observed differences to constrain the  
732 jet energy scale and its associated uncertainties.



733

## 734 JET ENERGY RESPONSE AND UNCERTAINTY

## 735 9.1 MOTIVATION

736 As jets form a major component of many physics analyses at ATLAS, it is cru-  
 737 cial to carefully calibrate the measurement of jet energies and to derive an un-  
 738 certainty on that measurement. These uncertainties have often been the dom-  
 739 inant systematic uncertainty in high-energy analyses at the Large Hadron Col-  
 740 linder ([LHC](#)). Dijet and multijet balance techniques provide a method to constrain  
 741 the [JES](#) and its uncertainty in data, and provide the default values used for ATLAS  
 742 jet measurements at most energies [30]. These techniques are limited by their re-  
 743 liance on measuring jets in data, so they are statistically limited in estimating  
 744 the jet energy scale at the highest jet energies. This chapter presents another  
 745 method for estimating the jet energy scale and its uncertainty which builds up a  
 746 jet from its components and thus can be naturally extended to high jet momen-  
 747 tum. Throughout this chapter the jets studied are simulated using [Pythia8](#) with  
 748 the CT10 parton distribution set [31] and the AU2 tune [8], and corrections are  
 749 taken from the studies including data and simulation in Chapter 8.

750 As described in Section 7.2, jets are formed from topological clusters of energy  
 751 in the calorimeters using the anti- $k_t$  algorithm. These clusters originate from a  
 752 diverse spectrum of particles, in terms of both species and momentum, leading to  
 753 significantly varied jet properties and response between jets of similar produced  
 754 momentum. Figure 19 shows the simulated distribution of particles within jets  
 755 at a few examples energies. The  $E/p$  measurements provide a thorough under-  
 756 standing of the dominant particle content of jets, the charged hadrons.

## 757 9.2 UNCERTAINTY ESTIMATE

758 Simulated jets are not necessarily expected to correctly model the energy de-  
 759 posits in the calorimeters, because of the various discrepancies discussed in Chap-  
 760 ter 8. To evaluate a jet energy response, the simulated jet energies are compared  
 761 to a corrected jet built up at the particle level. Each cluster in a jet is associated  
 762 to the truth particle which deposited it, and the energy in that cluster is then  
 763 corrected for a number of effects based on measurements in data. The primary  
 764 corrections come from the single hadron response measurements in addition  
 765 to response measured using the combined test beam which covers higher mo-  
 766 mentum particles [32]. These corrections include both a shift ( $\Delta$ ), in order to  
 767 make the simulation match the average response in data, and an uncertainty ( $\sigma$ )  
 768 associated with the ability to constrain the difference between data and simula-  
 769 tion. Some of the dominant sources of uncertainty are itemized in Table 1 with  
 770 typical values, and the full list considered is described in detail in the associated

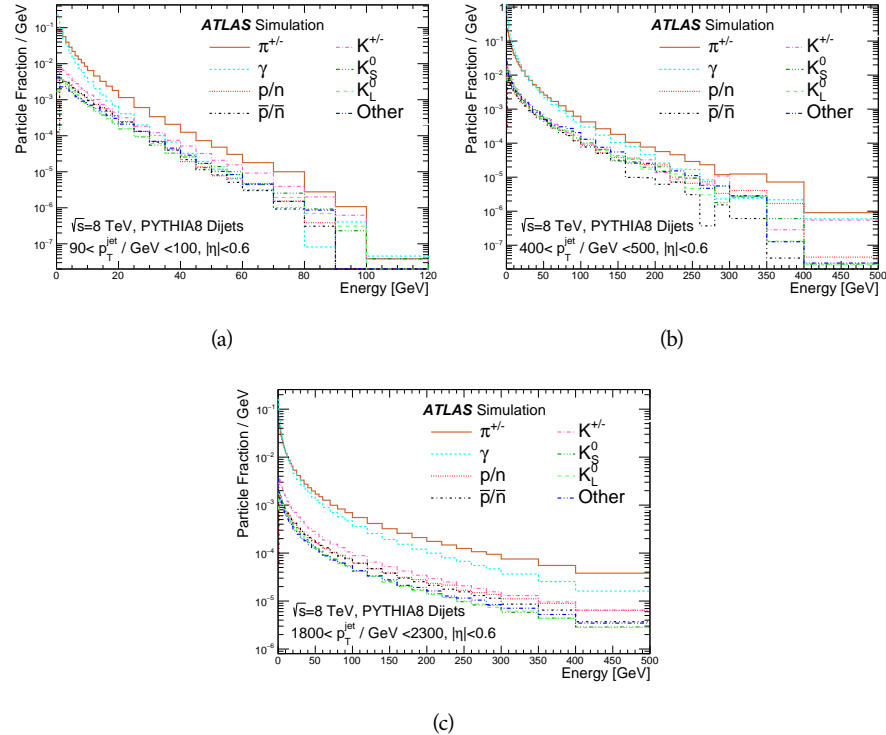


Figure 19: The spectra of true particles inside anti- $k_t$ ,  $R = 0.4$  jets with (a)  $90 < p_T/\text{GeV} < 100$ , (b)  $400 < p_T/\text{GeV} < 500$ , and (c)  $1800 < p_T/\text{GeV} < 2300$ .

paper [4]. These uncertainties cover differences between the data and simulation in the modeling of calorimeter response to a given particle. No uncertainties are added for the difference between particle composition of jets in data and simulation.

From these terms, the jet energy scale and uncertainty is built up from individual energy deposits in simulation. Each uncertainty term is treated independently, and are taken to be gaussian distributed. The resulting scale and uncertainty is shown in Figure 20, where the mean response is measured relative to the calibrated energy reported by simulation. The dominant uncertainties come from the statistical uncertainties on the  $E/p$  measurements at lower energies and the additional uncertainty for out of range measurements at higher energies. The total uncertainty from this method at intermediate jet energies is comparable to other simulation-based methods [33] and is about twice as large as in-situ methods using data [30]. This method is the only one which provides an estimation above 1.8 TeV, however, and so is still a crucial technique in analyses that search for very energetic jets.

These techniques can also be used to measure the correlation between bins of average reconstructed jet momentum across a range of  $p_T$  and  $|\eta|$ , where correlations are expected because of a similarity in particle composition at similar energies. Figure 21 shows these correlations, where the uncertainties on jets in neighboring bins are typically between 30% and 60% correlated. The uncertainty on all jets becomes significantly correlated at high energies and larger pseudora-

Abbrev.	Description	$\Delta$ (%)	$\sigma$ (%)
In situ $E/p$	The comparison of $\langle E/p \rangle_{\text{COR}}$ as described in Chapter 8 with statistical uncertainties from 500 MeV to 20 GeV.	0-3	1-5
CTB	The main $\langle E/p \rangle$ comparison uncertainties, binned in $p$ and $ \eta $ , as derived from the combined test beam results, from 20 to 350 GeV [32].	0-3	1-5
$E/p$ Zero Fraction	The difference in the zero-fraction between data and MC simulation from 500 MeV to 20 GeV.	5-25	1-5
$E/p$ Threshold	The uncertainty in the EM calorimeter response from the potential mismodeling of threshold effects in topological clustering.	0	0-10
Neutral	The uncertainty in the calorimeter response to neutral hadrons based on studies of physics model variations.	0	5-10
$K_L$	An additional uncertainty in the response to neutral $K_L$ in the calorimeter based on studies of physics model variations.	0	20
$E/p$ Misalignment	The uncertainty in the $p$ measurement from misalignment of the ID.	0	1
Hadrons, $p > 350$ GeV	A flat uncertainty for all particles above the energy range or outside the longitudinal range probed with the combined test beam.	0	10

Table 1: The dominant sources of corrections and systematic uncertainties in the [JES](#) estimation technique, including typical values for the correcting shift ( $\Delta$ ) and the associated uncertainty ( $\sigma$ ).

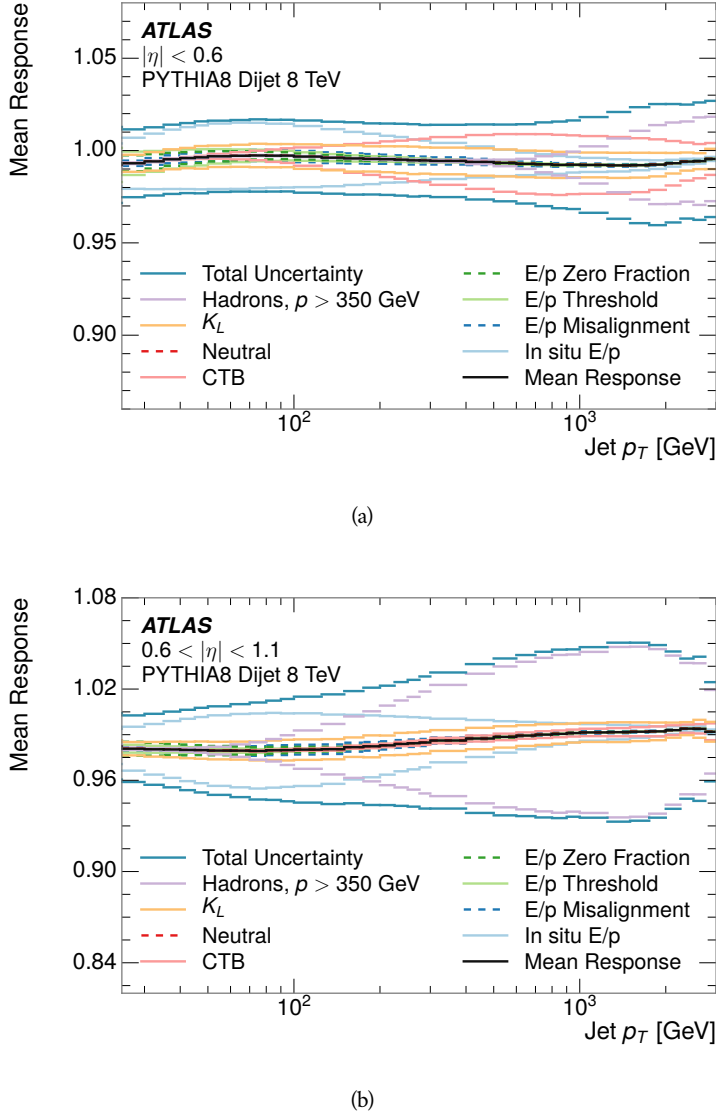


Figure 20: The [JES](#) uncertainty contributions, as well as the total [JES](#) uncertainty, as a function of jet  $p_T$  for (a)  $|\eta| < 0.6$  and (b)  $0.6 < |\eta| < 1.1$ .

793      pidities, when the uncertainty becomes dominated by the single term reflecting  
 794      out of range particles.

### 795      9.3 SUMMARY

796      The technique described above provides a jet energy scale and uncertainty by  
 797      building up jet corrections from the energy deposits of constituent particles. The  
 798       $E/p$  measurements are crucial in providing corrections for the majority of parti-  
 799      cles in the jets. The uncertainty derived this way is between 2 and 5% and is about  
 800      twice as large at corresponding momentum than jet balance methods. However  
 801      this is the only uncertainty available for very energetic jets using 2012 data and  
 802      simulation, and repeating this method with Run 2 data and simulation will be

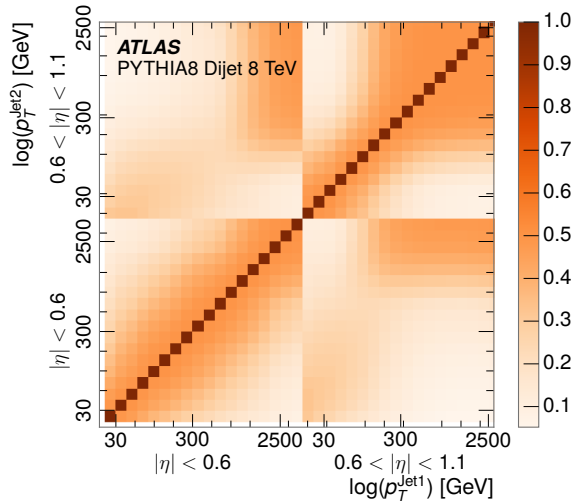


Figure 21: The JES correlations as a function of jet  $p_T$  and  $|\eta|$  for jets in the central region of the detector.

803 important in providing an uncertainty for the most energetic jets in 13 TeV col-  
 804 lisions.



805

## PART V

806

### SEARCH FOR LONG-LIVED PARTICLES

807

You can put some informational part preamble text here.



# 10

808

809 LONG-LIVED PARTICLES IN ATLAS

---

810 10.1 OVERVIEW AND CHARACTERISTICS

811 10.2 SIMULATION



812

813 EVENT SELECTION

---

814 The Long-Lived Particles ([LLPs](#)) targeted by this search differ in their interactions  
 815 with the detector from [SM](#) particles primarily because of their large mass. When  
 816 produced at the energies available at the [LHC](#), that large mass results in a low  $\beta$   
 817 and such slow-moving particles heavily ionize in detector material. Each layer  
 818 of the pixel detector provides a measurement of that ionization, through time  
 819 over threshold ([ToT](#)), as discussed in Section [6.3.1](#). The ionization in the pixel  
 820 detector, quantified in terms of  $dE/dx$ , provides the major focus for this search  
 821 technique, both for its discriminating power and also because of the large range  
 822 of lifetimes where it can be used. The  $dE/dx$  variable needs to be augmented  
 823 with a few additional selection requirements to form a complete search.

824 Ionization is not currently available in any form during triggering, so this  
 825 search instead relies on  $E_T^{\text{miss}}$  to trigger signal events. Although triggering on  
 826  $E_T^{\text{miss}}$  is not particularly efficient,  $E_T^{\text{miss}}$  is often large for many production mech-  
 827 anisms of [LLPs](#), as discussed in Section [10.1](#).

828 Ionization is most effective in rejecting backgrounds for well-measured, high-  
 829 momentum tracks, so some basic requirements on quality and kinematics are  
 830 placed on the particles considered in this search. In particular a newly intro-  
 831 duced tracking variable is very effective in removing highly-ionizing backgrounds  
 832 caused by overlapping tracks. A few additional requirements are placed on the  
 833 tracks considered for [LLP](#) candidates that increase background rejection by tar-  
 834 geting specific types of [SM](#) particles. These techniques provide a significant anal-  
 835 ysis improvement over previous iterations of ionization-based searches on AT-  
 836 LAS by providing additional background rejection with minimal loss in signal  
 837 efficiency.

838 The ionization measurement with the Pixel detector can be calibrated to pro-  
 839 vide an estimator of  $\beta\gamma$ . That estimate, together with the momentum measure-  
 840 ment provided by tracking, can be used to reconstruct a mass for each track  
 841 which traverses the pixel detector. That mass variable will be peaked at the [LLP](#)  
 842 mass for any signal, and provides an additional tool to search for an excess. In  
 843 addition to an explicit requirement on ionization, this search constructs a mass-  
 844 window for each targeted mass range in order to evaluate any excess of events  
 845 and to set limits.

846 The strategy discussed here is optimized for lifetimes of  $O(1) - O(10)$  ns.  
 847 Pixel ionization is especially useful in this regime as particles only need to prop-  
 848 agate through the first seven layers of the inner detector, about 37 cm from the  
 849 beam axis. The search is still competitive with other searches for [LLPs](#) at longer  
 850 lifetimes, because the primary discriminating variables are still applicable even  
 851 for particles that do not decay within the detector [34]. Although the basic strat-  
 852 egy remains the same for all lifetimes, two signal regions are defined to optimize  
 853 separately for intermediate and long lifetime particles.

## 854 11.1 TRIGGER

855 Triggering remains a significant difficulty in defining an event selection with  
 856 high signal efficiency in a search for [LLPs](#). There are no triggers available in  
 857 the current ATLAS system that can fire directly from a high momentum track  
 858 with large ionization (Section 6.6). Although in some configurations a charged  
 859 [LLP](#) can fire muon triggers, this requirement introduces significant model depen-  
 860 dence on both the allowed lifetimes and the interactions in the calorimeter [35].

861 For a search targetting particles which may decay prior to reaching the muon  
 862 system, the most efficient available trigger is based on missing energy [35]. As  
 863 discussed in Section 10.1, signal events can produce  $E_T^{\text{miss}}$  by two primary mech-  
 864 anisms. The decays of R-Hadrons to neutralinos can produce missing energy  
 865 when the neutralinos go undetected in the calorimeters. [LLPs](#) which do not de-  
 866 cay before the calorimeters also can produce missing energy because they do not  
 867 deposit much energy. Either case to some extent relies on kinematic degrees of  
 868 freedom to produce missing energy, as the pair-produced [LLPs](#) tend to balance  
 869 each other in the transverse plain. That balance results in a relatively low ef-  
 870 ficiency for long-lifetime particles, roughly 40%, and efficiencies between 65%  
 871 and 95% for shorter lifetimes depending on both the mass and the lifetime.

## 872 11.2 KINEMATICS AND ISOLATION

873 After the trigger requirement, each event is required to have a primary vertex  
 874 reconstructed from at least two well-measured tracks in the inner detector, each  
 875 with  $p_T > 400$  MeV. If more than one such vertex exists, the primary vertex is  
 876 taken to be the one with the largest summed track momentum for all tracks as-  
 877 sociated to that vertex. The offline reconstructed  $E_T^{\text{miss}}$  is required to be above  
 878 130 GeV to additionally reject [SM](#) backgrounds. The transverse missing energy  
 879 is calculated using fully reconstructed and calibrated offline objects, as described  
 880 in Section 7.5. In particular the  $E_T^{\text{miss}}$  definition in this selection uses jets recon-  
 881 structed with the anti- $k_t$  algorithm with radius  $R = 0.4$  from clusters of energy  
 882 in the calorimeter (Section 7.2) and with  $p_T > 20$  GeV, as well as reconstructed  
 883 muons, electrons, and tracks not identified as another object type.

884 The  $E_T^{\text{miss}}$  distributions are shown for data and a few simulated signals in Fig-  
 885 ure 22, after the trigger requirement. The cut placed at 130 GeV is 95% effi-  
 886 cient for metastable and 90% efficient for stable particles, because of the missing  
 887 energy generating mechanisms discussed previously. The distribution of data  
 888 in this figure and subsequent figures in this section can be interpreted as the  
 889 distribution of backgrounds, as any signal contamination would be negligible if  
 890 present at these early stages of the selection (prior to the final requirement on  
 891 mass). The background falls rapidly with missing energy, motivating the direct  
 892 requirement on  $E_T^{\text{miss}}$  for the signal region. Although a tigher requirement than  
 893 the specified value of 130 GeV would seem to increase the search potential from  
 894 these early distributions, other requirements are more optimal when taken as a  
 895 whole. The specific values for each requirement in signal region were optimized  
 896 considering the increase in discovery reach for tightening the requirement on

897 each discriminating variable. **NOTE: Is it interesting to discuss the signal re-  
898 gion optimization process in detail? I could add another section on how  
899 the values were determined, although in truth it is at least partially histor-  
900 ical precedence.**

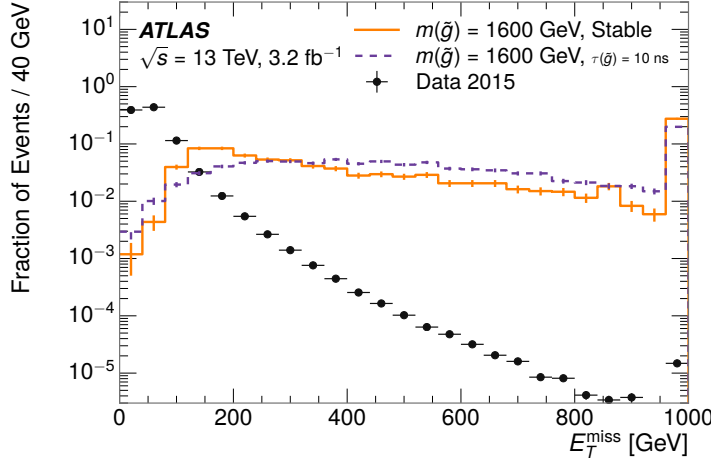


Figure 22: The distribution of  $E_T^{\text{miss}}$  for data and simulated signal events, after the trigger requirement.

901 Potential signal events are then required to have at least one candidate [LLP](#)  
902 track. Although the [LLPs](#) are produced in pairs, many models do not consistently  
903 yield two charged particles. For example, in the R-Hadron model highlighted  
904 here, only 20% of events have two charged R-Hadrons while 47% of events have  
905 just one. A signal region requiring two charged candidates could be a powerful  
906 improvement in background rejection for a larger dataset, but it is not consid-  
907 ered in this version of the analysis as it was found to be unnecessary to reject the  
908 majority of backgrounds.

909 For a track to be selected as a candidate, it must have  $p_T > 50 \text{ GeV}$  and pass  
910 basic quality requirements. The track must be associated to the primary vertex.  
911 It must also have at least seven clusters in the silicon layers in the inner detector  
912 to ensure an accurate measurement of momentum. Those clusters must include  
913 one in the innermost layer if the extrapolated track is expected to pass through  
914 that layer. And to ensure a reliable measurement of ionization, the track is re-  
915 quired to have at least two clusters in the pixel detector that provide a measure-  
916 ment of  $dE/dx$ .

917 At this point in the selection, there is a significant high-ionization background  
918 from multiple tracks that significantly overlap in the inner detector. Previous  
919 version of this analysis have rejected these overlaps by an explicit overlap rejec-  
920 tion between pairs of fully reconstructed tracks, typically by requiring no addi-  
921 tional tracks within a cone around the candidate. This technique, however, fails  
922 to remove the background from tracks that overlap so precisely that the tracks  
923 cannot be separately resolved.

924 A new method, added in Run 2, identifies cluster shapes that are likely formed  
925 by multiple tracks based on a neural network classification algorithm. The num-

926   ber of clusters that are classified this way in the pixel detector for a given track  
 927   is called  $N_{\text{split}}$ . As the shape of clusters requires significantly less spatial sepa-  
 928   ration to identify overlaps than it does to reconstruct two fully resolved tracks,  
 929   this variable is more effective at rejecting backgrounds from overlaps. Figure 23  
 930   shows the dependence of ionization on  $N_{\text{split}}$ ; as  $N_{\text{split}}$  increases the mean of  
 931    $dE/dx$  grows significantly up to twice the expected value when  $N_{\text{split}} = 4$ .

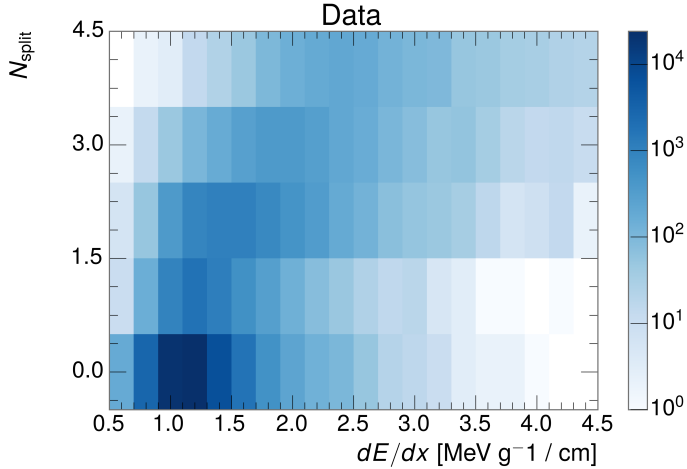


Figure 23: The dependence of  $dE/dx$  on  $N_{\text{split}}$  in data after basic track hit requirements have been applied.

932   This requirement is very successful in reducing the long positive tail of the  
 933    $dE/dx$  distributions, as can be seen in Figure 24. Comparing the distribution for  
 934   “baseline tracks”, tracks with only the above requirements on clusters applied and  
 935   before the requirement on  $N_{\text{split}}$ , to the distribution with  $N_{\text{split}} = 0$ , it is clear  
 936   that the fraction of tracks with large  $dE/dx$  is reduced by several orders of mag-  
 937   nitude. The isolated tracks are very close to the  $dE/dx$  distribution of identified  
 938   muons, which are extremely well isolated on average. Figure 24 also includes  
 939   the distribution of  $dE/dx$  in an example signal simulation to demonstrate how  
 940   effective  $dE/dx$  is as a discriminating variable with this isolation applied. The  
 941   background falls rapidly for  $dE/dx > 1.8 \text{ MeVg}^{-1}\text{cm}^2$  while the majority of  
 942   the signal, approximately 90% depending on the mass, falls above that threshold.  
 943   Over 90% of LLP tracks in simulated signal events pass the  $N_{\text{split}}$ -based isolation  
 944   requirement.

945   A few additional kinematic requirements are imposed to help reduce SM back-  
 946   grounds. The momentum of the candidate track must be at least 150 GeV, and  
 947   the uncertainty on that measurement must be less than 50%. The distribution of  
 948   momentum is shown in Figure 25 for tracks in data and simulated signal events  
 949   after the previously discussed requirements on clusters, transverse momentum,  
 950   and isolation have been imposed. The signal particles are much harder on aver-  
 951   age than their backgrounds because of the high energy interactions required to  
 952   produce them. The transverse mass,  $m_T$ , defined as

$$m_T = \sqrt{2 p_T E_T^{\text{miss}} (1 - \cos(\Delta\phi(E_T^{\text{miss}}, \text{track})))} \quad (1)$$

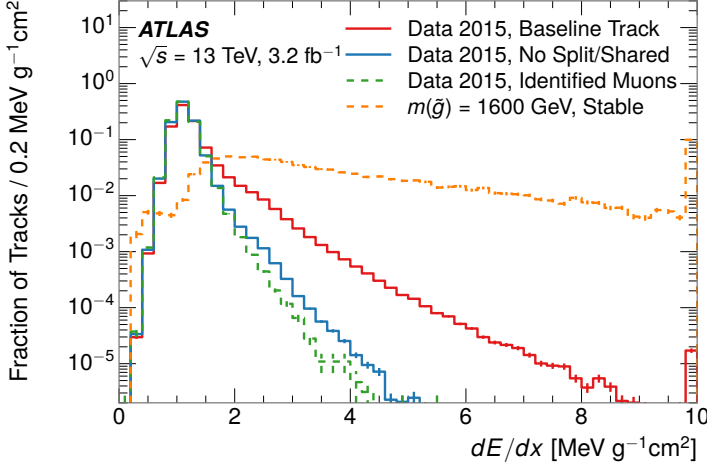


Figure 24: The distribution of  $dE/dx$  with various selections applied in data and simulated events.

estimates the mass of a decay of to a single charged particle and an undetected particle and is required to be greater than 130 GeV to reject contributions from the decay of W bosons. Figure 26 shows the distribution of  $m_T$  for data and simulated signal events. The signal is distributed over a wide range of  $m_T$ , with about 90% above the threshold value of 130 GeV. The data shows a dual-peaked structure, where the first peak comes from W boson decays and the second peak is a kinematic shaping from the requirements on  $E_T^{\text{miss}}$  and the track  $p_T$  in dijet events.

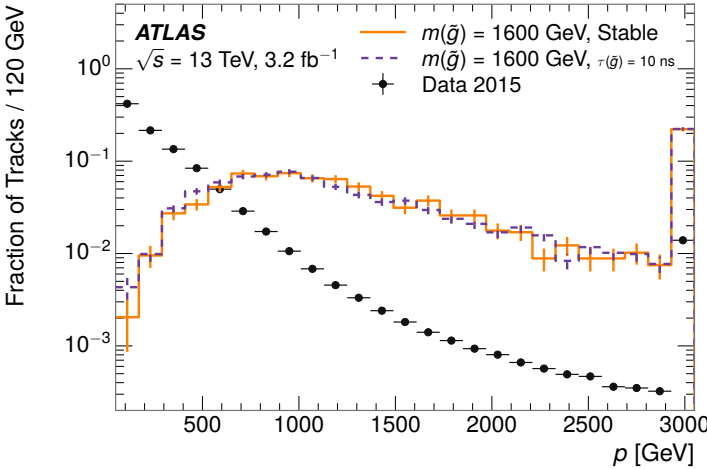


Figure 25: The distribution of track momentum for data and simulated signal events, after previous selection requirements have been applied.

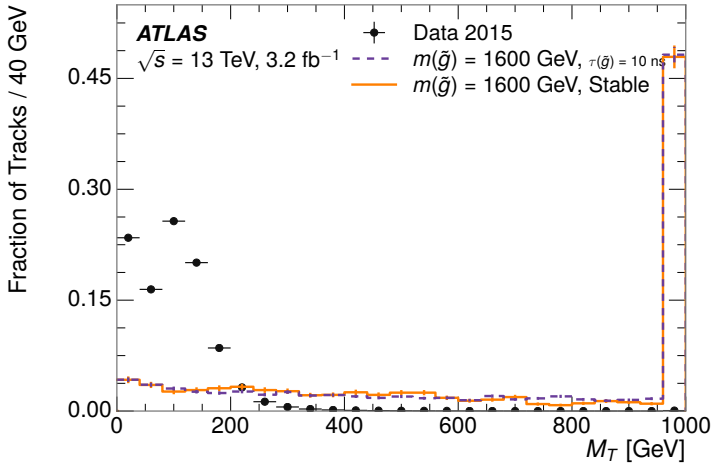


Figure 26: The distribution of  $M_T$  for data and simulated signal events, after previous selection requirements have been applied.

### 961 11.3 STANDARD MODEL REJECTION

962 Because the search selects events with just a single, highly-ionizing track, back-  
 963 grounds can be formed by a wide variety of SM processes when various charged  
 964 particles have a few randomly large deposits of energy in the pixel detector. Those  
 965 backgrounds can be effectively rejected by targeting the types of particles pro-  
 966 duced rather than the processes which produce them, as LLPs will have signifi-  
 967 cant differences compared to any SM particle. These rejections focus on using  
 968 additional features of the event, other than the kinematics or ionization of the  
 969 candidate track, as it provides a powerful source of background rejection with  
 970 very high signal efficiency. The lifetime of the particle can significantly change  
 971 its detector characteristics, as discussed in Section 10.1. To accomodate these  
 972 differences, the SM rejections defined in this section are split to form two signal  
 973 regions, one for long-lifetimes particles, the “stable” region, and one for interme-  
 974 diate lifetime particles, the “metastable” region.

975 Jets can be very effectively rejected by considering the larger-scale isolation of  
 976 the candidate track. In this case the isolation focuses on the production of nearby  
 977 particles as a jet-veto, rather than isolation from overlapping tracks to reduce  
 978 high-ionization backgrounds. As explained in Section 10.1, the fragmentation  
 979 process which produces an R-Hadron is very hard and thus is not expected to  
 980 produce additional particles. The jet-veto uses the summed momentum of tracks  
 981 with a cone of  $\Delta R < 0.25$ , referred to as  $p_T^{\text{Cone}}$ , which is shown in Figure 27 for  
 982 data and simulated signal events. In the data this value has a peak at zero from  
 983 isolated tracks such as leptons, and a long tail from jets which contains as much  
 984 as 80% of the background above 20 GeV at this stage of the selection. In signal  
 985 events  $p_T^{\text{Cone}}$  is strongly peaked at zero and significantly less than 1% is above 20  
 986 GeV. This makes a requirement of  $p_T^{\text{Cone}} < 20$  GeV one of the most effective  
 987 methods to reject background without losing signal efficiency. For the stable

988 signal region, this cut is further tightened to  $p_T^{\text{Cone}} < 5 \text{ GeV}$  as it is the most  
 989 effective variable remaining to extend the search reach for long lifetimes.

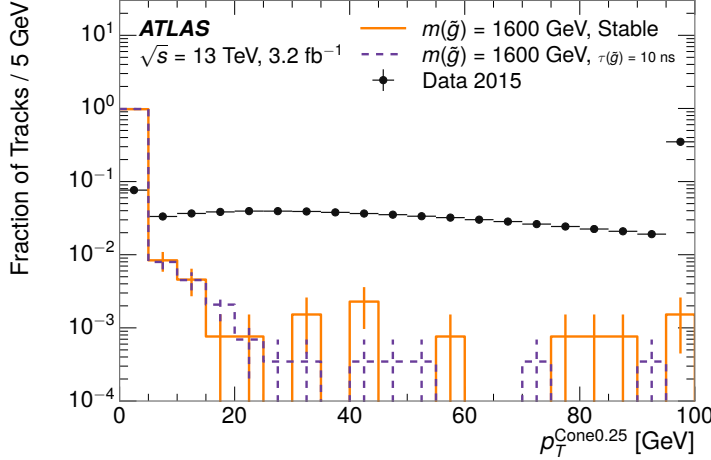


Figure 27: The distribution of summed tracked momentum within a cone of  $\Delta R < 0.25$  around the candidate track for data and simulated signal events, after previous selection requirements have been applied.

990 Even for fully isolated particles, there are additional methods to reject each  
 991 type of particle using information in the muon system and calorimeters. Muons  
 992 can be identified very reliably using the tracks in the muon system, as described  
 993 in Section 7.4. For intermediate lifetimes the LLPs do not survive long enough  
 994 to reach the muon system, and so muons are vetoed by rejecting tracks that as-  
 995 sociate to a muon with medium muon identification requirements. For longer  
 996 lifetimes, this rejection is not applied because LLPs which reach the muon system  
 997 can be identified as muons as often as 30% of the time in simulated samples.

998 Calorimeter-based particle rejection relies on the expected small deposits of  
 999 energy from LLPs. When the lifetime is long enough to reach the calorimeter, a  
 1000 LLP deposits little of its energy as it traverses the material, as discussed in Sec-  
 1001 tion 10.1. Even when the particle does decay before the calorimeter, the major-  
 1002 ity of its energy is carried away by the Lightest Supersymmetric Particle (LSP)  
 1003 and not deposited in the calorimeter. In both cases the energy is expected to be  
 1004 distributed across the layers of the calorimeters and not peaked in just one layer.  
 1005 This can be quantified in terms of  $E/p$ , the ratio of calorimeter energy of a nearby  
 1006 jet to the track momentum, and  $f_{\text{EM}}$ , the fraction of energy in that jet within the  
 1007 electromagnetic calorimeter. When no jets fall within a cone of 0.05 of the par-  
 1008 ticle,  $E/p$  and  $f_{\text{EM}}$  are both defined as zero.  $E/p$  is expected to be above 1.0  
 1009 for typical SM particles because of calibration and the contributions from other  
 1010 nearby particles. At these momenta there is no significant zero fraction due to  
 1011 interactions with the detector or insufficient energy deposits (see Section 8.2.2).  
 1012  $f_{\text{EM}}$  is peaked close to 1.0 for electrons, and distributed between 10% and 90%  
 1013 for hadrons.

1014 These trends can be seen in the two dimensional distribution for signal in Fig-  
 1015 ure 28 for stable and metastable (10 ns) events. The majority of R-Hadrons in

1016 both samples fall into the bin for  $E/p = 0$  and  $f_{EM} = 0$  because the majority of  
 1017 the time there is no associated jet. In the stable sample, when there is an associ-  
 1018 ated jet,  $E/p$  is typically still below 0.1, and the  $f_{EM}$  is predominantly under 0.8.  
 1019 In the metastable sample, on the other hand,  $E/p$  is larger but still typically below  
 1020 0.1 because of actual jets produced during the decay. The  $f_{EM}$  is much lower on  
 1021 average in this case, below 0.1, because the 10 ns lifetime particles rarely decay  
 1022 before passing through the electromagnetic calorimeter. Figure 28 also includes  
 1023 simulated Z decays to electrons or tau leptons. From the decays to electrons it is  
 1024 clear that the majority of electrons have  $f_{EM}$  above 0.9. The tau decays include a  
 1025 variety of products. Muons can be seen in the bin where  $E/p = 0$  and  $f_{EM} = 0$   
 1026 because they do not have an associated jet. Electrons fall into the range where  
 1027  $E/p > 1$  and  $f_{EM} > 0.9$ . Hadronic tau decays are the most common, and fall in  
 1028 the range of  $0.1 < f_{EM} < 0.9$  and  $E/p > 1.0$ .

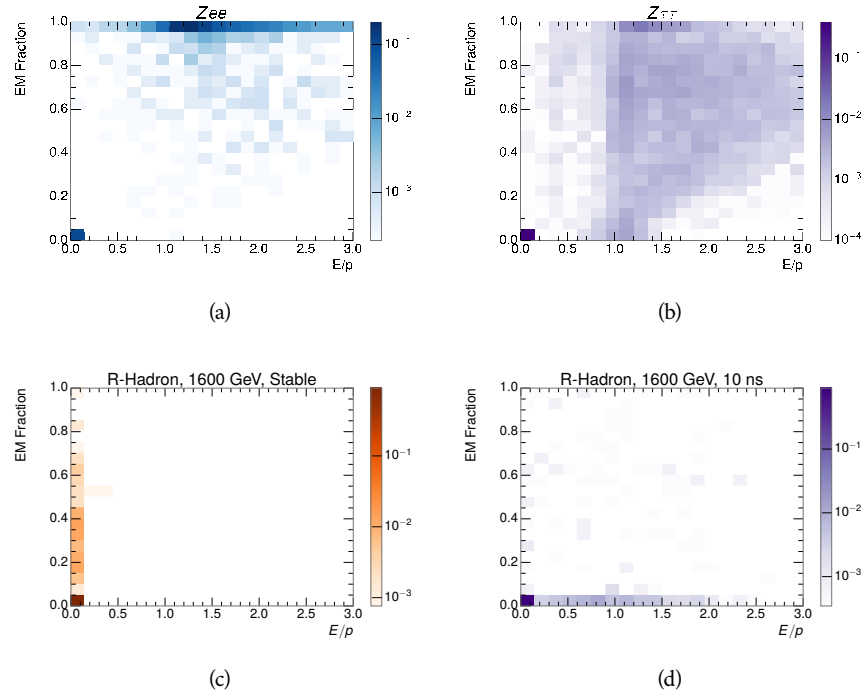


Figure 28: The normalized, two-dimensional distribution of  $E/p$  and  $f_{EM}$  for simulated  
 (a)  $Z \rightarrow ee$ , (b)  $Z \rightarrow \tau\bar{\tau}$ , (c) 1200 GeV Stable R-Hadron events, and (d) 1200  
 GeV, 10 ns R-Hadron events.

1029 These differences motivate an electron rejection by requiring an  $f_{EM}$  below  
 1030 0.9. Similarly, isolated hadrons are rejected by requiring  $E/p < 1.0$ . These re-  
 1031 quirements combine to remove the majority of isolated electrons and hadrons  
 1032 but retain over 95% of the simulated signal across a range of masses and lifetimes.

## 1033 11.4 IONIZATION

1034 The final requirements on the candidate track are the primary discriminating  
 1035 variables, the ionization in the pixel detector and the corresponding mass. That

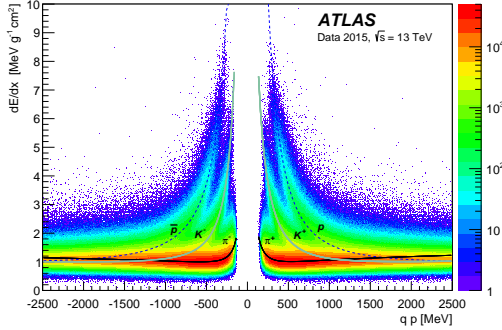


Figure 29: Two-dimensional distribution of  $dE/dx$  versus charge signed momentum ( $qp$ ) for minimum-bias tracks. The fitted distributions of the most probable values for pions, kaons and protons are superimposed.

ionization is measured in terms of  $dE/dx$ , which was shown for data and simulated signal events in Figure 24.  $dE/dx$  is dramatically greater for the high mass signal particles than the backgrounds, which start to fall immediately after the minimally ionizing peak at  $1.1 \text{ MeVg}^{-1}\text{cm}^2$ . The  $dE/dx$  for candidate tracks must be greater than a pseudorapidity-dependent threshold, specifically  $1.80 - 0.11|\eta| + 0.17\eta^2 - 0.05|\eta|^3 \text{ MeV g}^{-1} \text{ cm}^{-2}$ , in order to correct for an approximately 5% dependence of the MIP peak on  $\eta$ . The requirement was chosen as part of the signal region optimization, and manages to reduce the backgrounds by a factor of 100 while remaining 70-90% efficient for simulated signal events depending on the mass.

#### 11.4.1 MASS ESTIMATION

The mean value of ionization in silicon is governed by the Bethe-Bloch formula and the most probable value follows a Landau-Vavilov distribution [36]. Those forms inspire a parametric description of  $dE/dx$  in terms of  $\beta\gamma$ ,

$$(dE/dx)_{\text{MPV}}(\beta\gamma) = \frac{p_1}{\beta^{p_3}} \ln(1 + [p_2\beta\gamma]^{p_5}) - p_4 \quad (2)$$

which performs well in the range  $0.3 < \beta\gamma < 1.5$ . This range includes the expected range of  $\beta\gamma$  for the particles targeted for this search, with  $\beta\gamma \approx 2.0$  for lower mass particles ( $O(100 \text{ GeV})$ ) and up to  $\beta\gamma \approx 0.5$  for higher mass particles ( $O(1000 \text{ GeV})$ ). The parameters,  $p_i$ , are fit using a 2015 data sample of low-momentum pions, kaons, and protons as described in Ref. [37]. Figure 29 shows the two-dimensional distribution of  $dE/dx$  and momentum along with the above fitted values for  $(dE/dx)_{\text{MPV}}$ .

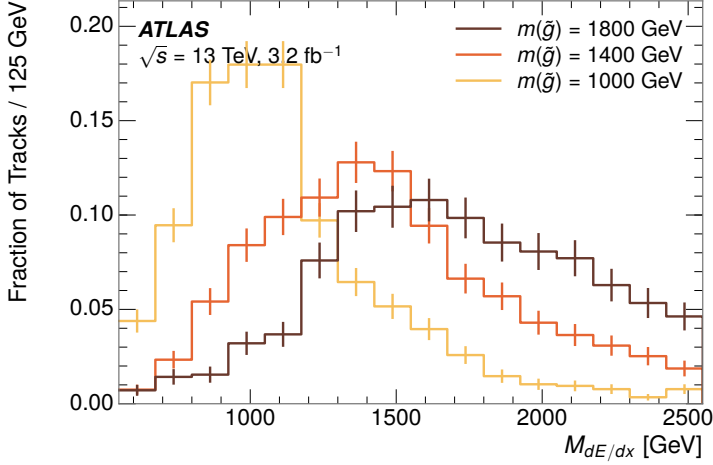


Figure 30: The distribution of mass estimated using  $dE/dx$  for simulated stable R-Hadrons with masses between 1000 and 1600 GeV.

The above equation (2) is then numerically inverted to estimate  $\beta\gamma$  and then mass for each candidate track. In simulated signal events, the mean of this mass value reproduces the generated mass up to around 1800 GeV to within 3%, and 3% shift is applied to correct for this difference. The mass distributions prior to this correction are shown for a few stable mass points in Figure 30. The large widths of these distributions come from the high variability in energy deposits in the pixel detector, but the means converge to the expected values.

This analysis evaluates expected yields and the resulting cross sectional limits using windows in this mass variable. The windows are formed by fitting mass distributions like those in Figure 30 to Gaussian distribution and taking all events that fall within  $\pm 1.4\sigma$  of the mean. As can be seen in Figure 30, typical values for this width are  $\sigma \approx 300 - 500$  GeV depending on the generated mass.

## 11.5 EFFICIENCY

The numbers of events passing each requirement through ionization are shown in Table 2 for the full 2015 dataset and a simulated 1600 GeV, 10 ns lifetime R-Hadron sample. The table highlights the overall acceptance  $\times$  efficiency for signal events, which for this example is 19%. Between SM rejection and ionization, this signal region reduces the background of tracks which pass the kinematic requirements down by an additional factor of almost 2000.

There is a strong dependence of this efficiency on lifetime and mass, with efficiencies dropping to under 1% at low lifetimes. Figure 31 shows the dependence on both mass and lifetime for all signal samples considered in this search. The dependence on mass is relatively slight and comes predominantly from the increasing fraction of R-Hadrons which pass the ionization cut with increasing mass. The trigger and  $E_T^{\text{miss}}$  requirements are most efficient for particles that decay before reaching the calorimeters. However, the chance of a particle to be

Selection	Exp. Signal Events	Observed Events in $3.2 \text{ fb}^{-1}$
Generated	$26.0 \pm 0.3$	
$E_T^{\text{miss}}$ Trigger	$24.8 \pm 0.3$ (95%)	
$E_T^{\text{miss}} > 130 \text{ GeV}$	$23.9 \pm 0.3$ (92%)	
Track Quality and $p_T > 50$	$10.7 \pm 0.2$ (41%)	368324
Isolation Requirement	$9.0 \pm 0.2$ (35%)	108079
Track $p > 150 \text{ GeV}$	$6.6 \pm 0.2$ (25%)	47463
$m_T > 130 \text{ GeV}$	$5.8 \pm 0.2$ (22%)	18746
Electron and Hadron Veto	$5.5 \pm 0.2$ (21%)	3612
Muon Veto	$5.5 \pm 0.2$ (21%)	1668
Ionization Requirement	$5.0 \pm 0.1$ (19%)	11

Table 2: The expected number of events at each level of the selection for metastable  $1600 \text{ GeV}$ , 10 ns R-Hadrons, along with the number of events observed in data, for  $3.2 \text{ fb}^{-1}$ . The simulated yields are shown with statistical uncertainties only. The total efficiency  $\times$  acceptance is also shown for the signal.

reconstructed as a high-quality track decreases significantly at low lifetimes as the particle does not propagate sufficiently through the inner detector. These effects lead to a maximum in the selection efficiency for lifetimes around 10-30 ns.

The inefficiency of this signal region at short lifetimes comes almost exclusively from an acceptance effect, in that the particles do not reach the necessary layers of the SCT. This can be seen more clearly by defining a fiducial region which includes events with at least one R-Hadron that is produced with non-zero charge,  $p_T > 50 \text{ GeV}$ ,  $p > 150 \text{ GeV}$ ,  $|\eta| < 2.5$ , and a decay distance greater than 37 cm in the transverse plane. At short (1 ns) lifetimes, the acceptance into this region is as low as 4%. Once this acceptance is accounted for, the selection efficiency ranges from 25% at lifetimes of 1 ns up to 45% at lifetimes of 10 ns.

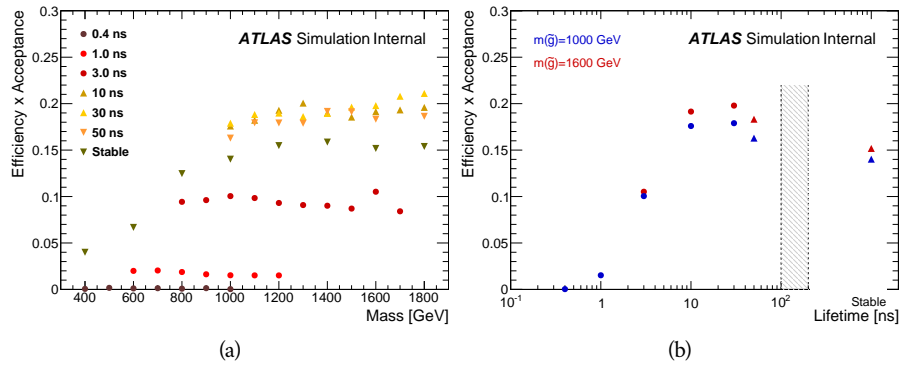


Figure 31: The acceptance  $\times$  efficiency as a function of R-Hadron (a) mass and (b) lifetime. (a) shows all of the combinations of mass and lifetime considered in this search, and (b) highlights the lifetime dependence for 1000 GeV and 1600 GeV R-Hadrons.

1095

1096 BACKGROUND ESTIMATION

---

1097 The event selection discussed in the previous section focuses on detector signa-  
 1098 tures, emphasizing a single high-momentum, highly-ionizing track. That track  
 1099 is then required to be in some way inconsistent with the expected properties  
 1100 of SM particles, with various requirements designed to reject jets, hadrons,  
 1101 electrons, and muons (Section 11.3). Were these selections perfectly effective, the sig-  
 1102 nal region would be entirely empty in data. So the background from this search  
 1103 comes entirely from reducible backgrounds that are outliers of various distribu-  
 1104 tions like momentum,  $dE/dx$ , and  $p_T^{\text{Cone}}$ . The simulation can be tuned in various  
 1105 ways to do an excellent job of modeling the average properties of each particle  
 1106 type [38], but it is not necessarily expected to accurately reproduce outliers. For  
 1107 these reasons, the background estimation used for this search is estimated en-  
 1108 tirely using data.

## 1109 12.1 BACKGROUND SOURCES

1110 Charged particles with lifetimes long enough to form tracks in the inner detector  
 1111 can be grouped into three major categories based on their detector interactions:  
 1112 hadrons, electrons, and muons. Every particle that enters into the background  
 1113 for this search belongs to one of these types. Relatively pure samples of each of  
 1114 these types can be formed in data by inverting the various rejection techniques  
 1115 in Section 11.3. Specifically, muons are selected requiring Medium muon iden-  
 1116 tification, electrons requiring  $E/p > 1.0$  and  $f_{\text{EM}} > 0.95$ , and hadrons requiring  
 1117  $E/p > 1.0$  and  $f_{\text{EM}} < 0.95$ .

1118 Figure 32 shows the distributions of momentum and  $dE/dx$  for these cate-  
 1119 gories in data, after requiring the event level selection as well as the track re-  
 1120 quirements on  $p_T$ , hits, and  $N_{\text{split}}$ , as discussed in Section 11.2. Simulated signal  
 1121 events are included for reference. These distribution are only illustrative of the  
 1122 differences between types, as the rejection requirements could alter their shape,  
 1123 especially for momentum which enters directly into  $E/p$  and can indirectly af-  
 1124 fect muon identification. However they do show a clear difference in both distri-  
 1125 butions. Momentum is expected to vary significantly because of the production  
 1126 mechanisms for the different species.  $dE/dx$  is different between types because  
 1127 of incomplete isolation; although the requirement on  $N_{\text{split}}$  helps to reduce the  
 1128 effect it does not completely remove the effect of overlaps. Muons are better  
 1129 isolated and thus have the smallest fraction of  $dE/dx$  above the threshold of 1.8  
 1130 MeVg $^{-1}$ cm $^2$ ; hadrons and electrons have a larger fraction above this threshold.

1131 It is difficult to determine what fraction of each particle type enters into the fi-  
 1132 nal signal region. The background method will not have significant dependence  
 1133 on the relative contributions of each species, but it is useful to understand the  
 1134 differences between each when considering the various tests of the method.

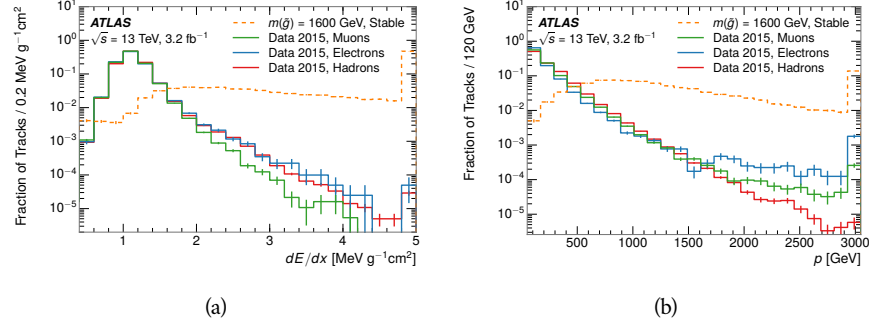


Figure 32: The distribution of (a)  $dE/dx$  and (b) momentum for tracks in data and simulated signal after requiring the event level selection and the track selection on  $p_T$ , hits, and  $N_{\text{split}}$ . Each subfigure shows the normalized distributions for tracks classified as hadrons, electrons, and muons in data and R-Hadrons in the simulated signal.

## 1135 12.2 PREDICTION METHOD

1136 The data-driven background estimation relies on the independence of ioniza-  
 1137 tion and other aspects of the event. For standard model particles with momenta  
 1138 above 50 GeV,  $dE/dx$  is not correlated with momentum. So, the proposed  
 1139 method to estimate the mass distribution of the signal region is to use momen-  
 1140 tumb from a track with low  $dE/dx$  (below the threshold value) and to combine it  
 1141 with a random  $dE/dx$  value from a  $dE/dx$  template. The resulting track is just  
 1142 as likely as the original, and so a number of such random generations forms a  
 1143 distribution of mass for the signal region.

1144 Algorithmically this method is implemented by forming two distinct Control  
 1145 Regions (**CRs**). The first **CR**, CR1, is formed by applying the entire event selection  
 1146 from Chapter 11 up to the  $dE/dx$  and mass requirements. The  $dE/dx$  require-  
 1147 ment is instead inverted for this region. Because of the independence of  $dE/dx$ ,  
 1148 the tracks in this control region have the same kinematic distribution as the  
 1149 tracks in the signal region, and are used to measure a two-dimensional template  
 1150 of momentum and  $\eta$ . The second **CR**, CR2, is formed from the event selection  
 1151 through the  $dE/dx$  requirement, but with an inverted  $E_T^{\text{miss}}$  requirement. The  
 1152 tracks in this control region are expected to have similar  $dE/dx$  distributions  
 1153 to the signal region, and so this region is used to measure a two-dimensional  
 1154 template of  $dE/dx$  and  $\eta$ .

1155 The contribution of any signal to the control regions is minimized by the in-  
 1156 verted selection requirements. Only less than 10% of simulated signal events  
 1157 have either  $dE/dx$  or  $E_T^{\text{miss}}$  below the threshold values in the original signal re-  
 1158 gion, while the backgrounds are significantly enhanced by inverting those re-  
 1159 quirements. The signal contamination is less than 1% in both control regions  
 1160 for all of the simulated masses and lifetimes considered in this analysis.

1161 With those measured templates, the shape of the mass estimation is generated  
 1162 by first selecting a random  $p, \eta$  combination from CR1. This momentum value is  
 1163 combined with a  $dE/dx$  value taken from the appropriate distribution of  $dE/dx$

1164 for the selected  $\eta$  from CR2. The use of  $\eta$  in both random samplings controls for  
1165 any correlation between  $p$ ,  $dE/dx$ , and  $\eta$ . Those values are then used to calculate  
1166 a mass in the same way that is done for regular tracks in data, see Section 11.4.1.  
1167 As this procedure includes all  $dE/dx$  values, the cut at  $1.8\text{MeVg}^{-1}\text{cm}^2$  is then  
1168 enforced to fully model the signal region. The generated mass distribution is  
1169 then normalized by scaling the background estimate to the data in the region  
1170  $M < 160\text{ GeV}$ , where signals of this type have already been excluded [39]. This  
1171 normalization takes place before the ionization requirement.

## 1172 12.3 VALIDATION

1173 The validity of the background estimation can be evaluated in both data and sim-  
1174 ulation. The underlying assumptions, that random combinations of  $dE/dx$  and  
1175 momentum can predict a mass distribution in another region, can be tested us-  
1176 ing simulated samples where concerns like multiple particle types can be con-  
1177 trolled. Using the same technique in another set of signal-depleted regions in  
1178 data then extends this confidence to the more complicated case where several  
1179 particle species are inherently included.

### 1180 12.3.1 CLOSURE IN SIMULATION

### 1181 12.3.2 VALIDATION REGION IN DATA



# 13

1182

1183 SYSTEMATIC UNCERTAINTIES AND RESULTS

---

1184 13.1 SYSTEMATIC UNCERTAINTIES

1185 13.2 FINAL YIELDS



# 14

1186

## 1187 INTERPRETATION

---

1188 14.1 CROSS SECTIONAL LIMITS

1189 14.2 MASS LIMITS

1190 14.3 CONTEXT FOR LONG-LIVED SEARCHES



1191

## PART VI

1192

### CONCLUSIONS

1193

You can put some informational part preamble text here.



# 15

1194

1195 SUMMARY AND OUTLOOK

---

1196 15.1 SUMMARY

1197 15.2 OUTLOOK



1198

## PART VII

1199

## APPENDIX

1200



# A

1201

1202 INELASTIC CROSS SECTION

---



# B

1203

## 1204 APPENDIX TEST

---

1205 Examples: *Italics*, SMALL CAPS, ALL CAPS <sup>1</sup>. Acronym testing: **UML!** (**UML!**) –  
1206 **UML! – UML! (UML!) – UML!s**

This appendix is temporary and is here to be used to check the style of the document.

### 1207 B.1 APPENDIX SECTION TEST

1208 Random text that should take up a few lines. The purpose is to see how sections  
1209 and subsections flow with some actual context. Without some body copy be-  
1210 tween each heading it can be difficult to tell if the weight of the fonts, styles, and  
1211 sizes use work well together.

#### 1212 B.1.1 APPENDIX SUBECTION TEST

1213 Random text that should take up a few lines. The purpose is to see how sections  
1214 and subsections flow with some actual context. Without some body copy be-  
1215 tween each heading it can be difficult to tell if the weight of the fonts, styles, and  
1216 sizes use work well together.

### 1217 B.2 A TABLE AND LISTING

1218 Curabitur tellus magna, porttitor a, commodo a, commodo in, tortor. Donec in-  
1219 terdum. Praesent scelerisque. Maecenas posuere sodales odio. Vivamus metus  
1220 lacus, varius quis, imperdiet quis, rhoncus a, turpis. Etiam ligula arcu, elemen-  
1221 tum a, venenatis quis, sollicitudin sed, metus. Donec nunc pede, tincidunt in,  
1222 venenatis vitae, faucibus vel, nibh. Pellentesque wisi. Nullam malesuada. Morbi  
1223 ut tellus ut pede tincidunt porta. Lorem ipsum dolor sit amet, consectetur adip-  
1224 iscing elit. Etiam congue neque id dolor.

1225 There is also a Python listing below Listing 1.

---

1 Footnote example.

LABITUR BONORUM PRI NO	QUE VISTA	HUMAN
fastidii ea ius	germano	demonstratea
suscipit instructior	titulo	personas
quaestio philosophia	facto	demonstrated

Table 3: Autem usu id.

## 1226 B.3 SOME FORMULAS

Due to the statistical nature of ionisation energy loss, large fluctuations can occur in the amount of energy deposited by a particle traversing an absorber element<sup>2</sup>. Continuous processes such as multiple scattering and energy loss play a relevant role in the longitudinal and lateral development of electromagnetic and hadronic showers, and in the case of sampling calorimeters the measured resolution can be significantly affected by such fluctuations in their active layers. The description of ionisation fluctuations is characterised by the significance parameter  $\kappa$ , which is proportional to the ratio of mean energy loss to the maximum allowed energy transfer in a single collision with an atomic electron:

*You might get unexpected results using math in chapter or section heads. Consider the pdfspacing option.*

$$\kappa = \frac{\xi}{E_{\max}} \quad (3)$$

$E_{\max}$  is the maximum transferable energy in a single collision with an atomic electron.

$$E_{\max} = \frac{2m_e\beta^2\gamma^2}{1 + 2\gamma m_e/m_x + (m_e/m_x)^2},$$

1227 where  $\gamma = E/m_x$ ,  $E$  is energy and  $m_x$  the mass of the incident particle,  $\beta^2 =$   
1228  $1 - 1/\gamma^2$  and  $m_e$  is the electron mass.  $\xi$  comes from the Rutherford scattering  
1229 cross section and is defined as:

$$\xi = \frac{2\pi z^2 e^4 N_{Av} Z \rho \delta x}{m_e \beta^2 c^2 A} = 153.4 \frac{z^2}{\beta^2} \frac{Z}{A} \rho \delta x \text{ keV},$$

1230 where

$z$  charge of the incident particle  
 $N_{Av}$  Avogadro's number  
 $Z$  atomic number of the material  
 $A$  atomic weight of the material  
 $\rho$  density  
 $\delta x$  thickness of the material  
 1232  $\kappa$  measures the contribution of the collisions with energy transfer close to  
 1233  $E_{\max}$ . For a given absorber,  $\kappa$  tends towards large values if  $\delta x$  is large and/or if  
 1234  $\beta$  is small. Likewise,  $\kappa$  tends towards zero if  $\delta x$  is small and/or if  $\beta$  approaches  
 1235 1.

2 Examples taken from Walter Schmidt's great gallery:  
<http://home.vrweb.de/~was/mathfonts.html>

Listing 1: A floating example (listings manual)

---

```
1 for i in xrange(10):
    print i, i*i, i*i*i
print "done"
```

---

1236      The value of  $\kappa$  distinguishes two regimes which occur in the description of  
1237      ionisation fluctuations:

- 1238      1. A large number of collisions involving the loss of all or most of the incident  
1239      particle energy during the traversal of an absorber.

1240      As the total energy transfer is composed of a multitude of small energy  
1241      losses, we can apply the central limit theorem and describe the fluctua-  
1242      tions by a Gaussian distribution. This case is applicable to non-relativistic  
1243      particles and is described by the inequality  $\kappa > 10$  (i. e., when the mean en-  
1244      ergy loss in the absorber is greater than the maximum energy transfer in  
1245      a single collision).

- 1246      2. Particles traversing thin counters and incident electrons under any condi-  
1247      tions.

1248      The relevant inequalities and distributions are  $0.01 < \kappa < 10$ , Vavilov  
1249      distribution, and  $\kappa < 0.01$ , Landau distribution.



1250 BIBLIOGRAPHY

---

- 1251 [1] S. Agostinelli et al. “GEANT4: A simulation toolkit”. In: *Nucl. Instrum. Meth.*  
1252 A 506 (2003), pp. 250–303. doi: [10.1016/S0168-9002\(03\)01368-8](https://doi.org/10.1016/S0168-9002(03)01368-8).
- 1253 [2] ATLAS Collaboration. “A study of the material in the ATLAS inner de-  
1254 tector using secondary hadronic interactions”. In: *JINST* 7 (2012), P01013.  
1255 doi: [10.1088/1748-0221/7/01/P01013](https://doi.org/10.1088/1748-0221/7/01/P01013). arXiv: [1110.6191 \[hep-ex\]](https://arxiv.org/abs/1110.6191).  
1256 [PERF-2011-08](#).
- 1257 [3] ATLAS Collaboration. “Electron and photon energy calibration with the  
1258 ATLAS detector using LHC Run 1 data”. In: *Eur. Phys. J. C* 74 (2014), p. 3071.  
1259 doi: [10.1140/epjc/s10052-014-3071-4](https://doi.org/10.1140/epjc/s10052-014-3071-4). arXiv: [1407.5063](https://arxiv.org/abs/1407.5063)  
1260 [hep-ex]. [PERF-2013-05](#).
- 1261 [4] ATLAS Collaboration. “A measurement of the calorimeter response to sin-  
1262 ggle hadrons and determination of the jet energy scale uncertainty using  
1263 LHC Run-1  $pp$ -collision data with the ATLAS detector”. In: (2016). arXiv:  
1264 [1607.08842 \[hep-ex\]](https://arxiv.org/abs/1607.08842). [PERF-2015-05](#).
- 1265 [5] ATLAS Collaboration. “Single hadron response measurement and calorime-  
1266 ter jet energy scale uncertainty with the ATLAS detector at the LHC”. In:  
1267 *Eur. Phys. J. C* 73 (2013), p. 2305. doi: [10.1140/epjc/s10052-013-2305-1](https://doi.org/10.1140/epjc/s10052-013-2305-1). arXiv: [1203.1302 \[hep-ex\]](https://arxiv.org/abs/1203.1302). [PERF-2011-05](#).
- 1269 [6] ATLAS Collaboration. “The ATLAS Simulation Infrastructure”. In: *Eur.*  
1270 *Phys. J. C* 70 (2010), p. 823. doi: [10.1140/epjc/s10052-010-1429-9](https://doi.org/10.1140/epjc/s10052-010-1429-9).  
1271 arXiv: [1005.4568 \[hep-ex\]](https://arxiv.org/abs/1005.4568). [SOFT-2010-01](#).
- 1272 [7] T. Sjöstrand, S. Mrenna, and P. Skands. “A Brief Introduction to PYTHIA  
1273 8.1”. In: *Comput. Phys. Commun.* 178 (2008), pp. 852–867. doi: [10.1016/j.cpc.2008.01.036](https://doi.org/10.1016/j.cpc.2008.01.036). arXiv: [0710.3820](https://arxiv.org/abs/0710.3820).
- 1275 [8] ATLAS Collaboration. *Summary of ATLAS Pythia 8 tunes*. ATL-PHYS-PUB-  
1276 2012-003. 2012. URL: <http://cds.cern.ch/record/1474107>.
- 1277 [9] A.D. Martin, W.J. Stirling, R.S. Thorne, and G. Watt. “Parton distributions  
1278 for the LHC”. In: *Eur. Phys. J. C* 63 (2009). Figures from the [MSTW Website](#),  
1279 pp. 189–285. doi: [10.1140/epjc/s10052-009-1072-5](https://doi.org/10.1140/epjc/s10052-009-1072-5). arXiv: [0901.0002](https://arxiv.org/abs/0901.0002).
- 1281 [10] A. Sherstnev and R.S. Thorne. “Parton Distributions for LO Generators”.  
1282 In: *Eur. Phys. J. C* 55 (2008), pp. 553–575. doi: [10.1140/epjc/s10052-008-0610-x](https://doi.org/10.1140/epjc/s10052-008-0610-x). arXiv: [0711.2473](https://arxiv.org/abs/0711.2473).
- 1284 [11] A. Ribon et al. *Status of Geant4 hadronic physics for the simulation of LHC*  
1285 *experiments at the start of LHC physics program*. CERN-LCGAPP-2010-02.  
1286 2010. URL: <http://lcgapp.cern.ch/project/docs/noteStatusHadronic2010.pdf>.

- 1288 [12] M. P. Guthrie, R. G. Alsmiller, and H. W. Bertini. "Calculation of the cap-  
 1289 ture of negative pions in light elements and comparison with experiments  
 1290 pertaining to cancer radiotherapy". In: *Nucl. Instrum. Meth.* 66 (1968), pp. 29–  
 1291 36. doi: [10.1016/0029-554X\(68\)90054-2](https://doi.org/10.1016/0029-554X(68)90054-2).
- 1292 [13] H. W. Bertini and P. Guthrie. "News item results from medium-energy  
 1293 intranuclear-cascade calculation". In: *Nucl. Instr. and Meth. A* 169 (1971),  
 1294 p. 670. doi: [10.1016/0375-9474\(71\)90710-X](https://doi.org/10.1016/0375-9474(71)90710-X).
- 1295 [14] V.A. Karmanov. "Light Front Wave Function of Relativistic Composite  
 1296 System in Explicitly Solvable Model". In: *Nucl. Phys. B* 166 (1980), p. 378.  
 1297 doi: [10.1016/0550-3213\(80\)90204-7](https://doi.org/10.1016/0550-3213(80)90204-7).
- 1298 [15] H. S. Fesefeldt. *GHEISHA program*. Pitha-85-02, Aachen. 1985.
- 1299 [16] G. Folger and J.P. Wellisch. "String parton models in Geant4". In: (2003).  
 1300 arXiv: [nucl-th/0306007](https://arxiv.org/abs/nucl-th/0306007).
- 1301 [17] N. S. Amelin et al. "Transverse flow and collectivity in ultrarelativistic  
 1302 heavy-ion collisions". In: *Phys. Rev. Lett.* 67 (1991), p. 1523. doi: [10.1103/PhysRevLett.67.1523](https://doi.org/10.1103/PhysRevLett.67.1523).
- 1304 [18] N. S. Amelin et al. "Collectivity in ultrarelativistic heavy ion collisions". In:  
 1305 *Nucl. Phys. A* 544 (1992), p. 463. doi: [10.1016/0375-9474\(92\)90598-E](https://doi.org/10.1016/0375-9474(92)90598-E).
- 1307 [19] L. V. Bravina et al. "Fluid dynamics and Quark Gluon string model - What  
 1308 we can expect for Au+Au collisions at 11.6 AGeV/c". In: *Nucl. Phys. A* 566  
 1309 (1994), p. 461. doi: [10.1016/0375-9474\(94\)90669-6](https://doi.org/10.1016/0375-9474(94)90669-6).
- 1310 [20] L. V. Bravin et al. "Scaling violation of transverse flow in heavy ion colli-  
 1311 sions at AGS energies". In: *Phys. Lett. B* 344 (1995), p. 49. doi: [10.1016/0370-2693\(94\)01560-Y](https://doi.org/10.1016/0370-2693(94)01560-Y).
- 1313 [21] B. Andersson et al. "A model for low-pT hadronic reactions with general-  
 1314 izations to hadron-nucleus and nucleus-nucleus collisions". In: *Nucl. Phys.*  
 1315 *B* 281 (1987), p. 289. doi: [10.1016/0550-3213\(87\)90257-4](https://doi.org/10.1016/0550-3213(87)90257-4).
- 1316 [22] B. Andersson, A. Tai, and B.-H. Sa. "Final state interactions in the (nuclear)  
 1317 FRITIOF string interaction scenario". In: *Z. Phys. C* 70 (1996), pp. 499–  
 1318 506. doi: [10.1007/s002880050127](https://doi.org/10.1007/s002880050127).
- 1319 [23] B. Nilsson-Almqvist and E. Stenlund. "Interactions Between Hadrons and  
 1320 Nuclei: The Lund Monte Carlo, Fritiof Version 1.6". In: *Comput. Phys. Com-*  
 1321 *mun.* 43 (1987), p. 387. doi: [10.1016/0010-4655\(87\)90056-7](https://doi.org/10.1016/0010-4655(87)90056-7).
- 1322 [24] B. Ganhuyag and V. Uzhinsky. "Modified FRITIOF code: Negative charged  
 1323 particle production in high energy nucleus nucleus interactions". In: *Czech.*  
 1324 *J. Phys.* 47 (1997), pp. 913–918. doi: [10.1023/A:1021296114786](https://doi.org/10.1023/A:1021296114786).
- 1325 [25] ATLAS Collaboration. "Topological cell clustering in the ATLAS calorime-  
 1326 ters and its performance in LHC Run 1". In: (2016). arXiv: [1603.02934](https://arxiv.org/abs/1603.02934)  
 1327 [*hep-ex*].
- 1328 [26] Peter Speckmayer. "Energy Measurement of Hadrons with the CERN AT-  
 1329 LAS Calorimeter". Presented on 18 Jun 2008. PhD thesis. Vienna: Vienna,  
 1330 Tech. U., 2008. URL: <http://cds.cern.ch/record/1112036>.

- 1331 [27] CMS Collaboration. “The CMS barrel calorimeter response to particle  
1332 beams from 2 to 350 GeV/c”. In: *Eur. Phys. J. C* 60.3 (2009). doi: [10.1140/epjc/s10052-009-0959-5](https://doi.org/10.1140/epjc/s10052-009-0959-5).
- 1334 [28] J. Beringer et al. (Particle Data Group). “Review of Particle Physics”. In:  
1335 *Chin. Phys. C* 38 (2014), p. 090001. URL: <http://pdg.lbl.gov>.
- 1336 [29] P. Adragna et al. “Measurement of Pion and Proton Response and Lon-  
1337 gitudinal Shower Profiles up to 20 Nuclear Interaction Lengths with the  
1338 ATLAS Tile Calorimeter”. In: *Nucl. Instrum. Meth. A* 615 (2010), pp. 158–  
1339 181. doi: [10.1016/j.nima.2010.01.037](https://doi.org/10.1016/j.nima.2010.01.037).
- 1340 [30] ATLAS Collaboration. “Jet energy measurement and its systematic uncer-  
1341 tainty in proton–proton collisions at  $\sqrt{s} = 7$  TeV with the ATLAS detec-  
1342 tor”. In: *Eur. Phys. J. C* 75 (2015), p. 17. doi: [10.1140/epjc/s10052-014-3190-y](https://doi.org/10.1140/epjc/s10052-014-3190-y). arXiv: [1406.0076 \[hep-ex\]](https://arxiv.org/abs/1406.0076). PERF-2012-01.
- 1344 [31] Hung-Liang Lai, Marco Guzzi, Joey Huston, Zhao Li, Pavel M. Nadolsky,  
1345 et al. “New parton distributions for collider physics”. In: *Phys. Rev. D* 82  
1346 (2010), p. 074024. doi: [10.1103/PhysRevD.82.074024](https://doi.org/10.1103/PhysRevD.82.074024). arXiv: [1007.2241 \[hep-ph\]](https://arxiv.org/abs/1007.2241).
- 1348 [32] E. Abat et al. “Study of energy response and resolution of the ATLAS barrel  
1349 calorimeter to hadrons of energies from 20 to 350 GeV”. In: *Nucl. Instrum.*  
1350 *Meth. A* 621.1-3 (2010), pp. 134 –150. doi: <http://dx.doi.org/10.1016/j.nima.2010.04.054>.
- 1352 [33] ATLAS Collaboration. “Jet energy measurement with the ATLAS detector  
1353 in proton–proton collisions at  $\sqrt{s} = 7$  TeV”. In: *Eur. Phys. J. C* 73 (2013),  
1354 p. 2304. doi: [10.1140/epjc/s10052-013-2304-2](https://doi.org/10.1140/epjc/s10052-013-2304-2). arXiv: [1112.6426 \[hep-ex\]](https://arxiv.org/abs/1112.6426). PERF-2011-03.
- 1356 [34] ATLAS Collaboration. “Search for heavy long-lived charged  $R$ -hadrons  
1357 with the ATLAS detector in  $3.2 \text{ fb}^{-1}$  of proton–proton collision data at  
1358  $\sqrt{s} = 13$  TeV”. In: *Phys. Lett. B* 760 (2016), pp. 647–665. doi: [10.1016/j.physletb.2016.07.042](https://doi.org/10.1016/j.physletb.2016.07.042). arXiv: [1606.05129 \[hep-ex\]](https://arxiv.org/abs/1606.05129).
- 1360 [35] A. C. Kraan, J. B. Hansen, and P. Nevski. “Discovery potential of R-hadrons  
1361 with the ATLAS detector”. In: *Eur. Phys. J. C* 49 (2007), pp. 623–640. doi:  
1362 [10.1140/epjc/s10052-006-0162-x](https://doi.org/10.1140/epjc/s10052-006-0162-x). arXiv: [hep-ex/0511014 \[hep-ex\]](https://arxiv.org/abs/hep-ex/0511014).
- 1364 [36] K. A. Olive et al. “Review of Particle Physics”. In: *Chin. Phys. C* 38 (2014),  
1365 p. 090001. doi: [10.1088/1674-1137/38/9/090001](https://doi.org/10.1088/1674-1137/38/9/090001).
- 1366 [37] “dE/dx measurement in the ATLAS Pixel Detector and its use for particle  
1367 identification”. In: (2011).
- 1368 [38] ATLAS Collaboration. “The ATLAS Simulation Infrastructure”. In: *Eur.*  
1369 *Phys. J. C* 70 (2010), pp. 823–874. doi: [10.1140/epjc/s10052-010-1429-9](https://doi.org/10.1140/epjc/s10052-010-1429-9). arXiv: [1005.4568 \[physics.ins-det\]](https://arxiv.org/abs/1005.4568).

- <sup>1371</sup> [39] ATLAS Collaboration. “Search for metastable heavy charged particles with  
<sup>1372</sup> large ionisation energy loss in  $p\bar{p}$  collisions at  $\sqrt{s} = 8$  TeV using the AT-  
<sup>1373</sup> LAS experiment”. In: *Eur. Phys. J. C* 75 (2015), p. 407. doi: [10.1140/epjc/s10052-015-3609-0](https://doi.org/10.1140/epjc/s10052-015-3609-0). arXiv: [1506.05332 \[hep-ex\]](https://arxiv.org/abs/1506.05332). SUSY-  
<sup>1374</sup> 2014-09.  
<sup>1375</sup>

1376 DECLARATION

---

1377 Put your declaration here.

1378 *Berkeley, CA, September 2016*

1379

---

Bradley Axen



1380

1381 COLOPHON

1382

Not sure that this is necessary.